The Astrophysical Journal, 985:248 (18pp), 2025 June 1 https://doi.org/10.3847/1538-4357/adcd74

SZ–X-Ray Surface Brightness Fluctuations in the SPT-XMM Clusters

Charles E. Romero[1], Massimo Gaspari[2], Gerrit Schellenberger[1], Bradford A. Benson[3,4,5], Lindsey E. Bleem[5,6], Esra Bulbul[7], William Forman[1], Ralph Kraft[1], Paul Nulsen[1,8], Christian L. Reichardt[9], Arnab Sarkar[10], Taweewat Somboonpanyakul[11], and Yuanyuan Su[12]
[1] Center for Astrophysics | Harvard & Smithsonian, 60 Garden Street, Cambridge, MA 02138, USA; charles.romero@gmail.com
[2] Department of Physics, Informatics & Mathematics, University of Modena & Reggio Emilia, 41125 MO, Italy
[3] Fermi National Accelerator Laboratory, MS209, P.O. Box 500, Batavia, IL 60510, USA
[4] Department of Astronomy and Astrophysics, University of Chicago, 5640 South Ellis Avenue, Chicago, IL 60637, USA
[5] Kavli Institute for Cosmological Physics, University of Chicago, 5640 South Ellis Avenue, Chicago, IL 60637, USA
[6] High Energy Physics Division, Argonne National Laboratory, 9700 South Cass Avenue, Lemont, IL 60439, USA
[7] Max Planck Institute for Extraterrestrial Physics, Giessenbachstrasse 1, 85748 Garching, Germany
[8] ICRAR, University of Western Australia, 35 Stirling Highway, Crawley, WA 6009, Australia
[9] School of Physics, University of Melbourne, Parkville, VIC 3010, Australia
[10] Kavli Institute for Astrophysics and Space Research, Massachusetts Institute of Technology, 70 Vassar Street, Cambridge, MA 02139, USA
[11] Department of Physics, Faculty of Science, Chulalongkorn University, 254 Phayathai Road, Pathumwan, Bangkok 10330, Thailand
[12] Department of Physics and Astronomy, University of Kentucky, 505 Rose Street, Lexington, KY 40506, USA
Received 2024 December 5; revised 2025 April 10; accepted 2025 April 12; published 2025 May 29

Abstract

The hot plasma in galaxy clusters, the intracluster medium, is expected to be shaped by subsonic turbulent motions, which are key for heating, cooling, and transport mechanisms. The turbulent motions contribute to the nonthermal pressure, which, if not accounted for, consequently imparts a hydrostatic mass bias. Accessing information about turbulent motions is thus of major astrophysical and cosmological interest. Characteristics of turbulent motions can be indirectly accessed through surface brightness fluctuations. This study expands on our pilot investigations of surface brightness fluctuations in the Sunyaev–Zel'dovich and in X-ray data by examining, for the first time, a large sample of 60 clusters using both SPT-SZ and XMM-Newton data and spans the redshift range $0.2 < z < 1.5$, thus constraining the respective pressure and density fluctuations within $0.6R_{500}$. We deem density fluctuations to be of sufficient quality for 32 clusters, finding mild correlations between the peak of the amplitude spectra of density fluctuations and various dynamical parameters. We infer turbulent velocities from density fluctuations with an average Mach number $\mathcal{M}_{3D} = 0.52 \pm 0.14$, in agreement with numerical simulations. For clusters with inferred turbulent Mach numbers from fluctuations in both pressure, $\mathcal{M}_P$, and density, $\mathcal{M}_\rho$, we find broad agreement between $\mathcal{M}_P$ and $\mathcal{M}_\rho$. Our results suggest either a bimodal or a skewed unimodal Mach number distribution, with the majority of clusters being turbulence-dominated (subsonic) while the remainder are shock-dominated (supersonic).

Unified Astronomy Thesaurus concepts: Intracluster medium (858); Galaxy clusters (584)

1. Introduction

The dominant baryonic component of galaxy clusters is the hot (10^7–10^8 K) intracluster medium (ICM). The thermal component of the ICM is observable via X-rays and in the millimeter band via the Sunyaev–Zel'dovich (SZ) effect (R. A. Sunyaev & Y. B. Zel'dovich 1972), while relativistic particles are observable via synchrotron radiation at lower frequencies. The thermal gas, especially at moderate to large radii ($\sim R_{2500}$ to R_{500}),[13] matches well expectations of self-similarity and gravitational heating (see, e.g., A. V. Kravtsov & S. Borgani 2012). Gravitational heating is likely to proceed primarily through shock (adiabatic) heating or turbulent (dissipative) heating. Through numerical simulations X. Shi et al. (2020) found that turbulent heating should be dominant within R_{500}, while shock heating (especially for accretion shocks) will dominate at $r > R_{500}$.

In the central regions of galaxy clusters, baryonic physics is critical. In particular, radiative cooling appears to be self-regulated via active galactic nuclei (AGN) feedback (e.g., B. R. McNamara & P. E. J. Nulsen 2012; M. Gaspari et al. 2014a; G. M. Voit et al. 2017). In the case of merger shocks and AGN feedback, much of the gas heating will be localized and yet the balanced feedback requires much of the energy to be isotropically distributed throughout the ICM, with turbulence likely playing a crucial role in this transport (e.g., D. Wittor & M. Gaspari 2020, 2023). At the same time, turbulence is expected to have a prominent role in gas condensation in cluster centers, driving chaotic cold accretion onto supermassive black holes (M. Gaspari et al. 2020, for a review), as well as in the reacceleration of cosmic rays, generating extended radio emission (G. Brunetti & T. W. Jones 2014; D. Eckert et al. 2017; R. J. van Weeren et al. 2019; T. Pasini et al. 2024).

Beyond the inextricable role that turbulence plays in the thermodynamics of the ICM, it will also impart a nonthermal pressure component throughout the ICM and thereby contribute to the hydrostatic mass bias,[14] which is currently the

[13] For a density contrast, Δ, R_Δ is the radius within which the mean matter density is Δ times the critical density of the Universe.

[14] The hydrostatic mass bias is the bias on a mass estimate when assuming that the cluster is in hydrostatic equilibrium and thus only supported by thermal pressure.

dominant source of systematic uncertainty in mass estimation from the ICM (see G. W. Pratt et al. 2019, for a recent review).

Despite the integral role that turbulence must play in the observed X-ray, millimeter, and radio signals, constraining turbulence—especially turbulent motions—has not come easily (e.g., A. Simionescu et al. 2019). While there is much anticipation of constraints on turbulent velocity from Doppler shifts and broadening of lines in high-resolution X-ray spectroscopy via the recently launched XRISM (XRISM Science Team 2020) and proposed facilities such as the Line Emission Mapper (R. Kraft et al. 2022), Athena (N. Meidinger et al. 2012; K. Nandra et al. 2013; A. Rau et al. 2013), and now NewAthena (M. Cruise et al. 2025) turbulent velocities can also be accessed via the driven surface brightness fluctuations in the X-ray (e.g., P. Schuecker et al. 2004; E. Churazov et al. 2012; M. Gaspari & E. Churazov 2013; M. Gaspari et al. 2014b; F. Hofmann et al. 2016; A. Heinrich et al. 2024) and SZ images (R. Khatri & M. Gaspari 2016; C. E. Romero et al. 2023). From a cosmological perspective, constraining turbulent motions in the cluster outskirts (at radii of roughly R_{500} and larger) is most important. As both SZ and X-ray signals are faint (relative to the cluster cores), such observations are expensive. Moreover, the relative expense of velocity constraints from high-resolution X-ray spectroscopy compared to surface brightness fluctuations (e.g., C. E. Romero 2024) suggests that measuring turbulence in the cluster outskirts is more feasible via surface brightness fluctuations.

Accessing surface brightness fluctuations via both X-rays and the SZ effect can be desirable for their different observational properties, i.e., advantages, as well as their different physical insights, where they are best suited to constraining density and pressure fluctuations, respectively. With both density and pressure fluctuations, one can assess the effective equation of state (C. E. Romero et al. 2023) and potentially more robustly constrain the turbulent gas velocities.

Given the sensitivity required to obtain meaningful constraints on density and pressure fluctuations, we may also be interested in correlating those fluctuations with other, more accessible parameters. While AGN feedback should generate turbulence in the central regions (e.g., D. Wittor & M. Gaspari 2023), this is not expected to be dominant at moderate ($r > R_{2500c}$) clustercentric radii (e.g., E. T. Lau et al. 2017). If merger activity is expected to be the primary driver of gas motion at moderate radii and larger, then we can expect some degree of correlation with typical dynamical parameters (e.g., L. Lovisari et al. 2017; Z. S. Yuan et al. 2022).

The sample selection and approach, building on the pilot study of C. E. Romero et al. (2024), are discussed in Section 2. We present results in Section 3 and discuss them in Section 4. Our assumed cosmology adopts $H_0 = 70\,\mathrm{km\,s^{-1}\,Mpc^{-1}}$, $\Omega_M = 0.3$, and $\Omega_\Lambda = 0.7$. We report all uncertainties as one standard deviation (for distributions taken to be symmetric) or the distance from the median to the 16th and 84th percentiles (when allowing for asymmetric distributions), unless otherwise stated.

2. Approach

We seek to constrain density and pressure fluctuations via X-ray and SZ observations, respectively. Unlike previous studies, we aim to have a large statistical sample across a wide mass and redshift range (see Figure 1). To do this, we use a sample defined by the galaxy clusters in the SPT-SZ survey

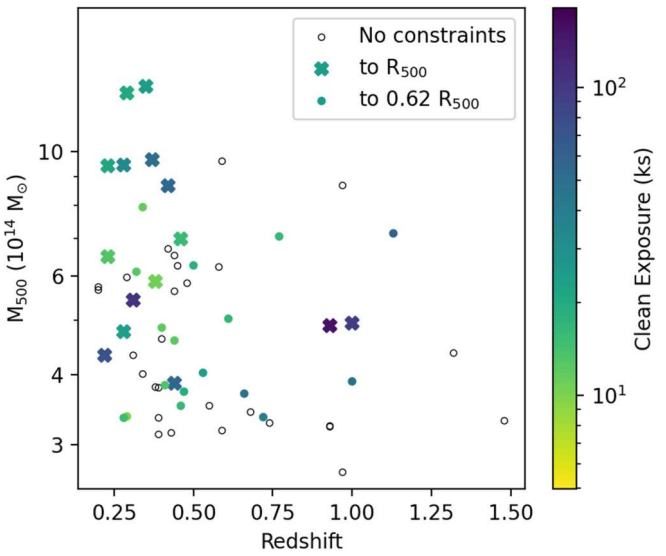

Figure 1. The mass and redshift distribution of clusters in our (SPT-XMM) sample as well as information regarding constraints on surface brightness fluctuations from XMM-Newton data. Empty circles denote no significant constraints are reported; filled markers denote that constraints of at least 2σ were obtained within $0.62R_{500}$ (filled circles) and out to R_{500} (crosses). The color indicates a representative exposure time across the EPIC cameras.

(L. E. Bleem et al. 2015) that also have sufficiently deep XMM-Newton data. Such a sample was compiled by E. Bulbul et al. (2019). SPT-CLJ0014-3022 was observed with the South Pole Telescope (SPT) camera (T. Plagge et al. 2010) separately from the SPT-SZ survey. Given that SPT-CLJ0014-3022 (also called A2744) meets the criteria on redshift ($z > 0.2$) and photon count (more than 1000 filtered source counts in MOS cameras) for the sample selection of E. Bulbul et al. (2019), it is also included in our sample, which we call the SPT-XMM sample. Additional properties of the sample are discussed in Appendix A.

2.1. Image and Fourier Analysis

Our data analysis approach follows that used in our precursory studies (R. Khatri & M. Gaspari 2016; C. E. Romero et al. 2024), which we summarize here. For surface brightness images, y and S, in the SZ and in X-rays, respectively, we fit smooth surface brightness models, $\bar{y}$ and $\bar{S}$, to their respective images. In this work, we take our models to be circular β models in both the SZ and X-ray cases, with the SZ and X-ray centers fixed to the centroid found in the X-ray data set. We also run the SZ profile fitting procedure with the center free to infer Δ_c, the SZ to X-ray centroid offset. The SZ model, $\bar{y}$, is entirely defined by the ICM; i.e., any mean level or background component is assumed to have been nulled. The X-ray model, $\bar{S}$, can be taken as the sum of an ICM component and a background component: $\bar{S} = \bar{S}_{\rm ICM} + \bar{S}_{\rm bkg}$ (C. E. Romero et al. 2023). Residual maps are taken to be $\delta y = y - \bar{y}$ and $\delta S = S - \bar{S}$. Point sources and chip gaps are masked as in previous analyses (C. E. Romero et al. 2023, 2024).

We characterize surface brightness fluctuations of the normalized residual maps, $\delta y/\bar{y}$ and $\delta S/\bar{S}_{\rm ICM}$, via a wavelet decomposition method based on a Mexican Hat filter (P. Arévalo et al. 2012). Like C. E. Romero et al. (2024), we adhere to exploring fluctuations in two regions: Ring 1, a circle of radius $0.62R_{500}$, and Ring 2, the annulus between $0.62R_{500}$ and R_{500}.

The power spectra of surface brightness fluctuations in the SZ and in X-rays are then deprojected to pressure and density fluctuations, characterized by their 3D spectra, P_{3D}, as done by C. E. Romero et al. (2024). The fluctuations may also be represented through their amplitude spectra:

$$A_{3D} = \sqrt{4\pi k^3 P_{3D}}. \quad (1)$$

Specifically, we calculate A_{3D} to correspond to density fluctuations, i.e., A_ρ, when considering X-ray data. Similarly, in the case of SZ data, A_{3D} is taken as A_P. We sample our spectra at angular scales between our resolution limit (taken to be $10''$ for XMM-Newton and $1.'25$ for SPT) and θ_{500} (the angular extent of R_{500} on the sky) with logarithmic spacing close to a factor of 2 so that each point is (approximately) independent.

2.1.1. X-Ray Image Processing and Spectral Coaddition

We extract images in the [0.4–1.25] keV and [2.0–5.0] keV bands for each of the EPIC cameras through the use of ESAS (S. L. Snowden et al. 2008), for each ObsID. As in our pilot study, a single cluster center and point-source mask is adopted across all images of a particular cluster. A β model is fit to each image, and fluctuation (normalized residual) images $S/\bar{S}_{ICM}$ are produced (for each band, camera, and ObsID). Power spectra are measured on each image following the delta variance method employed by P. Arévalo et al. (2012), and deprojected to power spectra of gas density as in our pilot study (C. E. Romero et al. 2024). These deprojected power spectra (per band, camera, and ObsID) are combined by taking the weighted average, for a given cluster.

In our pilot study, neither of the two clusters investigated had clear substructure in the XMM-Newton images, and we did not investigate masking substructure. In the full sample, we encountered SPT-CLJ0658-5556 (also known as the Bullet cluster), SPT-CLJ0304-4401, SPT-CLJ2023-5535, SPT-CLJ0014-3022, and SPT-CLJ0225-4155, which we identified as having significant substructure, and we mask the substructure according to an algorithm detailed in Appendix B.

2.1.2. SZ Analysis of SPT-SZ Clusters

Our analyses of SPT images proceed like those of C. E. Romero et al. (2024) with the exception of the analysis of SPT-CLJ0014-3022, which is not in the SPT-SZ survey. SPT images are taken as minimum-variance Compton y maps (L. E. Bleem et al. 2022).

2.1.3. SZ Analysis of SPT-SZ Clusters SPT-CLJ0014-3022

The data set for SPT-CLJ0014-3022 (T. Crawford et al. 2022) does not include half maps, but rather a single map out to large clustercentric radii. The map is tapered starting at roughly $3R_{500}$. Two point sources are evident in the map (both are beyond $2R_{500}$) and are masked.

A mean level is found at radii beyond R_{500} and is subtracted. A β model is then fit to the cluster and a power spectrum within Ring 1 can be calculated on the resultant $\delta y/\bar{y}$ image, which will include power from the noise. Power spectra are computed in six nonoverlapping regions with radius equivalent to Ring 1 spaced far from the cluster center. That is, for each region, i, a corresponding $(\delta y/\bar{y})_i$ map is computed by moving the center of the $\bar{y}$ model to the center of the region. From these power spectra of "noise realizations," we debias and derive uncertainties on the desired SZ surface brightness fluctuations.

3. Results

From pressure or density fluctuations, one can infer turbulent velocities quantified in relation to the sound speed, i.e., their Mach numbers (e.g M. Gaspari et al. 2014b; R. Khatri & M. Gaspari 2016; S. Dupourqué et al. 2023; C. E. Romero et al. 2023; A. Heinrich et al. 2024). In particular, one either integrates over the power spectrum (M. Simonte et al. 2022; I. Zhuravleva et al. 2023) and applies a linear relation to obtain a Mach number, or one finds the peak of the amplitude spectrum and applies a linear scaling from that peak to obtain a Mach number (M. Gaspari & E. Churazov 2013). As we do not always have good constraints at all scales of our power spectra, we opt to estimate Mach numbers from our defined peak of each amplitude spectrum. It is interesting to note that such a linear relation might appear a trivial result (first shown by M. Gaspari & E. Churazov 2013); however, this linearity only arises in stratified atmospheres (like the ICM), while a quadratic scaling is expected in pure hydrodynamics (E. Churazov et al. 2012).

Throughout this paper, we present Mach numbers in terms of 3D gas velocities, i.e., $\mathcal{M}_{3D}$. When these Mach numbers are (specifically) inferred from density and pressure fluctuations, we adopt the respective notations $\mathcal{M}_\rho$ and $\mathcal{M}_P$. At times we further specify which rings these values may pertain to with an additional index (subscript), e.g., for Ring 1: $\mathcal{M}_{\rho,1}$ and $\mathcal{M}_{P,1}$. To determine turbulent velocities, we adopt the relations from M. Gaspari & E. Churazov (2013):

$$\mathcal{M}_\rho = 4.0 A_\rho(k_{peak,\rho})\left(\frac{l_{inj}}{0.4R_{500}}\right)^{\alpha_H} \quad (2)$$

$$\mathcal{M}_P = 2.4 A_P(k_{peak,P})\left(\frac{l_{inj}}{0.4R_{500}}\right)^{\alpha_H}, \quad (3)$$

where l_{inj} is the injection scale and the parameter $\alpha_H = -0.25$ models the hydrodynamical regime of negligible thermal conduction, as expected in the ICM due to magnetic and plasma microscale processes (M. Gaspari et al. 2014b; J. A. ZuHone et al. 2015; S. V. Komarov et al. 2016).

We define the peak of A_ρ to be the maximum of the set of points with signal-to-noise ratio (SNR), $\xi_{A_\rho} = A_\rho/\sigma_{A_\rho}$, greater than 2 (amplitude spectra with at least one node $\xi > 9$ are shown in Appendix C). By extension, we define k_{peak} to be the wavenumber at which this peak is found. For a well-sampled and well-constrained amplitude spectrum, the inverse of the injection scale, $k_{inj} = 1/l_{inj}$, will effectively be the same as k_{peak}. However, our spectra are not well sampled, and thus we simply take k_{peak} as a proxy for k_{inj}.

Of the 60 clusters in our sample, 32 clusters yielded amplitude spectra of density fluctuations where a peak (as defined above) could be identified in Ring 1 and 15 clusters where such a peak could be identified in Ring 2. From the SZ side, only seven clusters are found to have a node in the amplitude spectra of Ring 1 above 1.5σ. In the following sections we focus on the results within Ring 1.

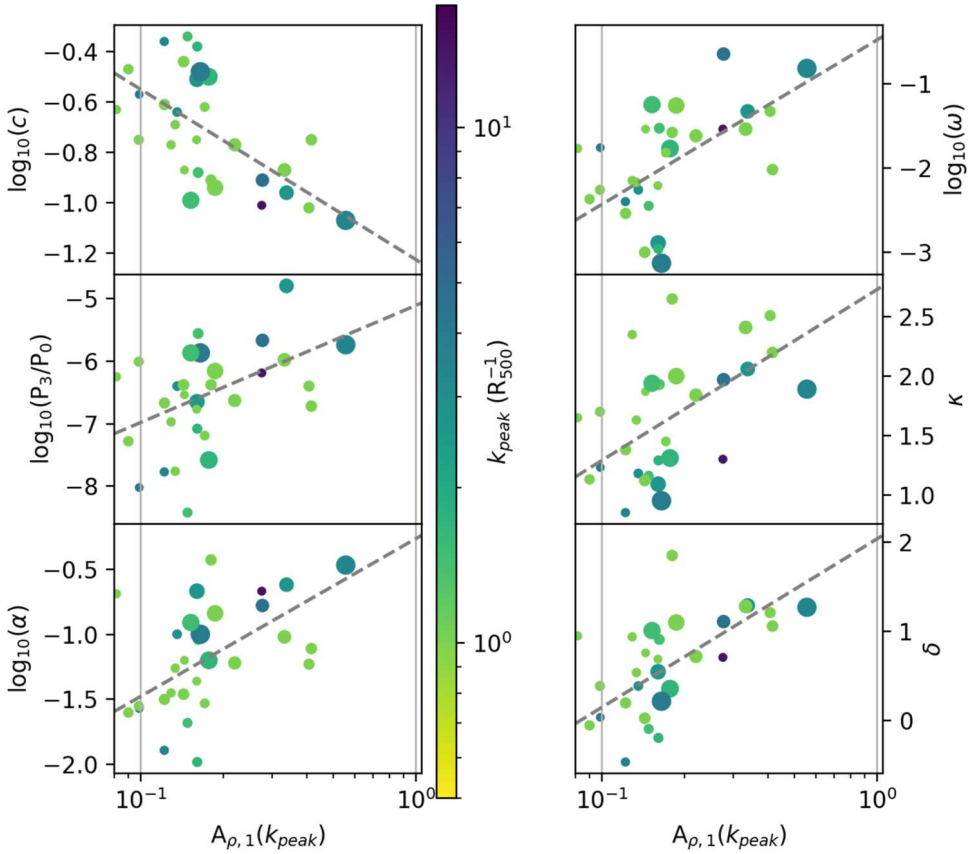

Figure 2. Scatter plots of dynamical parameters relative to the inferred A_ρ in Ring 1. Sizes of markers indicate the maximal ξ (see Appendix A) in $A_{\rho,1}$. The coloring of the markers corresponds to the location (wavenumber) of the inferred peak, adopting an SNR threshold of $\xi > 2$.

3.1. Correlations with Dynamical Parameters

As we may expect the inferred density fluctuations to be related to merger activity, we investigate correlations between the peak of the amplitude spectra of the inner rings (Ring 1) and the dynamical parameters as calculated by Z. S. Yuan et al. (2022). These parameters are c, P_3/P_0, α, ω, κ, and δ, which correspond to a concentration index, power ratio, asymmetry factor, peak–centroid offset, profile parameter, and morphology index, respectively. The quantitative formulae for these values are given by Z. S. Yuan et al. (2022). We take the values published in their table; some of the values are published as the base-10 logarithm of the above parameters, in which case we retain this logarithm.

Figures 2 and 3 show the retrieved correlations between the dynamical parameters and A_ρ or $\mathcal{M}_\rho$, respectively. The size of a marker in these figures corresponds to that maximal significance, ξ, in the amplitude spectrum for a given cluster. While the peak itself may be less significant, this is a means of indicating the overall quality of the data. The color of the points also indicates the inferred peak. The inferred peaks, although not strongly constrained, tend toward large scales ($0.5R_{500}$ to R_{500}).

Table 1 reports correlations between either A_ρ or $\mathcal{M}_\rho$ and the dynamical parameters cited above. We include an additional parameter, ΔR, we define as

$$\Delta R = \Delta_c/\theta_{500}, \tag{4}$$

where Δ_c is the angular distance between the SZ and X-ray centroids, and θ_{500} is the angular equivalent of R_{500}. We quantify the correlations with the Spearman and Pearson coefficients, $r_{\rm Sp}$ and $r_{\rm Pe}$, respectively. Additionally, we quantify the correlations via the linear correlation coefficient when considering a Bayesian approach with `LINMIX`[15] (B. C. Kelly 2007; M. Gaspari et al. 2019). This method takes observables y and x, the relations $y = \eta + \sigma_y$, $x = \xi_c + \sigma_x$, where ξ_c is the independent variable and η is the dependent variable, and fits the linear relation

$$\eta = \alpha_c + \beta_c \xi_c + \epsilon, \tag{5}$$

where ϵ is the intrinsic scatter and α_c and β_c are the regression coefficients. The correlation coefficient from `LINMIX` is that between ξ_c and η and is reported in Table 1 as $r_{\rm Lin}$. We report the coefficients α_c and β_c in Table 2.

S. Dupourqué et al. (2023) investigated correlations between the amplitude of fluctuations (related to the integral of the power spectrum of fluctuations), σ_δ, and dynamical parameters c, ω, the Gini coefficient, G, and an asymmetry parameter quantified through Zernike polynomials, C_Z. Although our comparisons are not precisely equivalent, we should expect that the correlations we find for $A_\rho(k_{\rm peak}) - \log_{10}(c)$ are similar to those found by S. Dupourqué et al. (2023) for $\sigma_\delta - c$ and likewise for $A_\rho(k_{\rm peak}) - \log_{10}(\omega)$ and their $\sigma_\delta - \omega$. This is in fact the case, where S. Dupourqué et al. (2023) find the Spearman coefficients for $\sigma_\delta - c$ and $\sigma_\delta - \omega$ to be $-0.4^{+0.15}_{-0.15}$ and $0.37^{+0.2}_{-0.18}$, respectively. Those values are similar to the analogous Spearman coefficients $-0.44^{+0.10}_{-0.08}$ and $0.48^{+0.08}_{-0.08}$

[15] As implemented in Python; see https://linmix.readthedocs.io/.

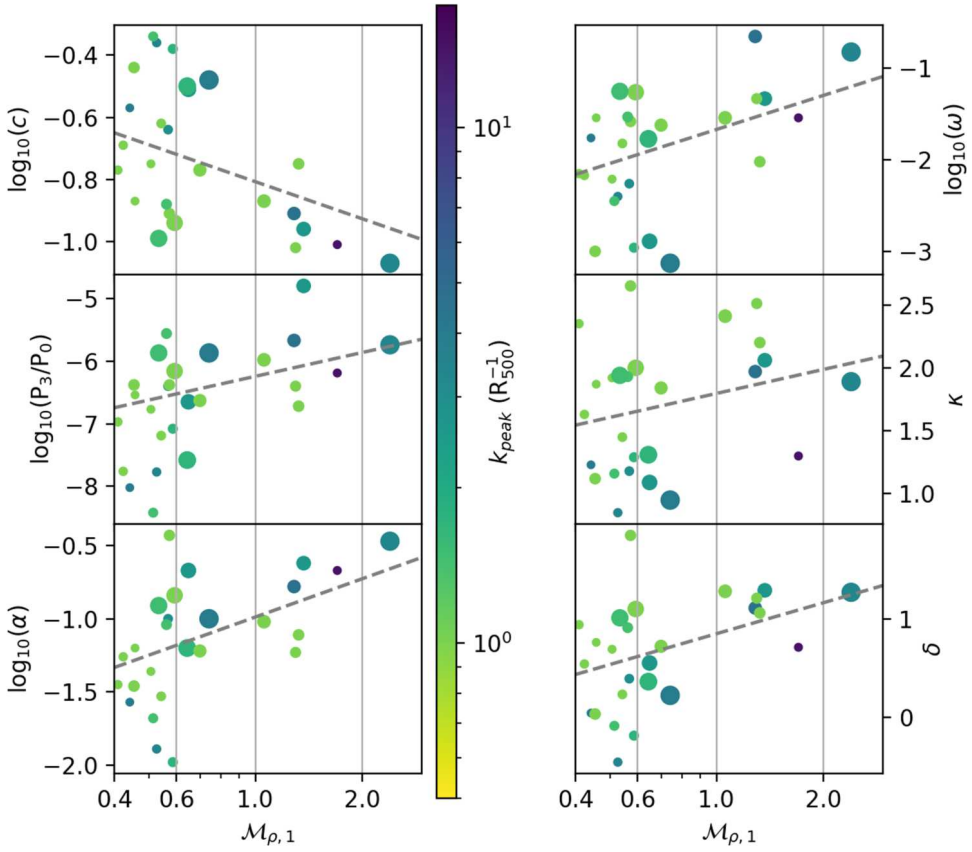

Figure 3. As for Figure 2, but relative to the inferred turbulent 3D Mach number $\mathcal{M}_\rho$ in Ring 1.

Table 1
Correlation Coefficients

Dynamical Parameter	$\log A_\rho$			$\log \mathcal{M}_\rho$		
	$r_{\rm Sp}$	$r_{\rm Pe}$	$r_{\rm Lin}$	$r_{\rm Sp}$	$r_{\rm Pe}$	$r_{\rm Lin}$
$\log c$	$-0.44^{+0.10}_{-0.08}$	$-0.43^{+0.09}_{-0.07}$	$-0.60^{+0.17}_{-0.14}$	$-0.34^{+0.05}_{-0.05}$	$-0.37^{+0.03}_{-0.04}$	$-0.39^{+0.19}_{-0.16}$
$\log \omega$	$0.48^{+0.08}_{-0.08}$	$0.44^{+0.06}_{-0.07}$	$0.59^{+0.13}_{-0.16}$	$0.40^{+0.04}_{-0.04}$	$0.40^{+0.02}_{-0.02}$	$0.42^{+0.15}_{-0.17}$
$\log\left(\frac{P_3}{P_0}\right)$	$0.34^{+0.11}_{-0.12}$	$0.34^{+0.10}_{-0.12}$	$0.50^{+0.17}_{-0.20}$	$0.34^{+0.08}_{-0.09}$	$0.35^{+0.07}_{-0.08}$	$0.40^{+0.17}_{-0.19}$
κ	$0.44^{+0.08}_{-0.10}$	$0.41^{+0.08}_{-0.09}$	$0.56^{+0.15}_{-0.17}$	$0.27^{+0.04}_{-0.04}$	$0.30^{+0.03}_{-0.03}$	$0.31^{+0.18}_{-0.19}$
$\log \alpha$	$0.43^{+0.09}_{-0.09}$	$0.42^{+0.08}_{-0.09}$	$0.57^{+0.15}_{-0.19}$	$0.51^{+0.04}_{-0.05}$	$0.44^{+0.03}_{-0.03}$	$0.45^{+0.15}_{-0.17}$
δ	$0.54^{+0.08}_{-0.09}$	$0.49^{+0.08}_{-0.09}$	$0.67^{+0.13}_{-0.17}$	$0.44^{+0.04}_{-0.04}$	$0.42^{+0.03}_{-0.03}$	$0.44^{+0.15}_{-0.18}$
ΔR	$-0.06^{+0.10}_{-0.10}$	$-0.03^{+0.09}_{-0.09}$	$-0.09^{+0.22}_{-0.22}$	$-0.14^{+0.06}_{-0.05}$	$-0.08^{+0.04}_{-0.04}$	$-0.08^{+0.20}_{-0.19}$

Note. Correlation coefficients obtained between either $\log A_\rho(k_{\rm peak})$ or $\log \mathcal{M}_\rho(k_{\rm peak})$ and various dynamical parameters with the cut $\xi_{A_\rho} > 2$.

reported in Table 1. S. Dupourqué et al. (2024) subdivided clusters into three bins of dynamical state based on ω and found a positive correlation with σ_δ, but provided no explicit calculation (correlation coefficient).

3.2. Correlations with the Mach Number

Where Table 1 presented the correlations of dynamical parameters relative to both A_ρ and $\mathcal{M}_\rho$ in Ring 1, and Figure 2 visually presented correlations against $A_{\rho,1}$, Figure 3 does so for $\mathcal{M}_{\rho,1}$. As evidenced in Table 1, the correlations do not differ drastically between the $A_{\rho,1}$ and $\mathcal{M}_{\rho,1}$ cases.

We considered additional correlations with $A_{\rho,1}$ or $\mathcal{M}_{\rho,1}$. There are several readily available quantities from previous works such as those of E. Bulbul et al. (2019), taken as the values within the aperture of R_{500}: $L_{\rm X,cin}$, $L_{\rm X,cin,bol}$, $T_{\rm X,cin}$, $Z_{\rm X,cin}$, $L_{\rm X,cex}$, $L_{\rm X,cex,bol}$, $T_{\rm X,cex}$, $Z_{\rm X,cex}$, $Y_{\rm X,cin}$, M_{500}, and z, where subscripts cin and cex indicate whether the core ($r < 0.15R_{500}$) is included or excised, respectively, for the quantities. We do not find any strong correlation among these variables and the inferred density fluctuations in Ring 1. The lack of correlation between luminosities, temperatures, and integrated Y relative to fluctuations is likely a symptom of the former quantities scaling with mass, whereas turbulence appears to be independent of mass (e.g., K. Nelson et al. 2014) or to have a mild dependence on it (e.g., N. Battaglia et al. 2012; M. Angelinelli et al. 2020). Even considering ratios of core-included to core-excluded quantities does not produce any strong correlations; this reinforces the notion that such ratios

Table 2
Linear Coefficients

Dynamical Parameter	$\log A_\rho$		$\log \mathcal{M}_\rho$	
	α_c	β_c	α_c	β_c
$\log c$	$-1.23^{+0.17}_{-0.16}$	$-0.69^{+0.22}_{-0.21}$	$-0.79^{+0.06}_{-0.05}$	$-0.35^{+0.17}_{-0.17}$
$\log \omega$	$-0.47^{+0.47}_{-0.47}$	$1.97^{+0.62}_{-0.62}$	$-1.72^{+0.16}_{-0.15}$	$1.07^{+0.46}_{-0.45}$
$\log\left(\frac{P_3}{P_0}\right)$	$-5.11^{+0.60}_{-0.59}$	$1.87^{+0.80}_{-0.76}$	$-6.25^{+0.18}_{-0.20}$	$1.25^{+0.61}_{-0.62}$
κ	$2.74^{+0.36}_{-0.36}$	$1.44^{+0.48}_{-0.47}$	$1.81^{+0.13}_{-0.13}$	$0.68^{+0.41}_{-0.41}$
$\log \alpha$	$-0.26^{+0.33}_{-0.32}$	$1.22^{+0.42}_{-0.41}$	$-1.01^{+0.10}_{-0.10}$	$0.78^{+0.31}_{-0.31}$
δ	$2.04^{+0.39}_{-0.39}$	$1.88^{+0.51}_{-0.51}$	$0.84^{+0.14}_{-0.13}$	$1.03^{+0.42}_{-0.41}$
ΔR	$0.06^{+0.06}_{-0.06}$	$-0.03^{+0.08}_{-0.09}$	$0.09^{+0.02}_{-0.02}$	$-0.03^{+0.06}_{-0.06}$

Note. Linear coefficients α_c and β_c, given in Equation (5), obtained between $\log A_\rho(k_{\rm peak})$ and various dynamical parameters with the cut $\xi_{A_\rho} > 2$.

are not robust tracers of dynamical state; e.g., cool cores can be present in both relaxed and disturbed systems.

From the SPT-SZ works (L. E. Bleem et al. 2015; S. Bocquet et al. 2019), one also has $Y_{\rm SZ}$. We therefore additionally consider the correlation of $Y_{\rm SZ}/Y_{\rm X,cin}$ and $A_{\rho,1}$, which yields no apparent correlation. Finally, we consider the self-similar scaling $Y_{\rm SZ} \propto E(s)^{2/3}M^{5/3}$ (e.g., A. V. Kravtsov & S. Borgani 2012) and compute a quantity $\Psi = Y_{\rm SZ}/(E(s)^{2/3}M_{500}^{5/3})$, which we then correlate against $A_{\rho,1}$. This too does not show a clear correlation. Of quantities that we have correlated with fluctuations ($A_{\rho,1}$) or the inferred turbulent Mach numbers ($\mathcal{M}_{\rho,1}$) those that we found to have statistically significant correlations are the dynamical parameters of Z. S. Yuan et al. (2022). We do not find significant difference among the correlation coefficients of these dynamical parameters (for a given comparison, e.g., against $A_{\rho,1}$). More sensitive measurements as well as a larger sample will help provide such distinctions.

3.3. Distribution of Fluctuations and Inferred Turbulent Velocities

The adopted threshold of 2σ ($\xi > 2$) is admittedly low and may introduce a bias due to noise that happens to scatter values above our threshold. Accounting for any bias is potentially quite involved, as there are at least two parts to consider: (1) what is the bias on the value of the amplitude spectrum at the considered wavenumber ($k_{\rm peak}$), and (2) would a correction to this bias change the inferred $k_{\rm peak}$? An earnest attempt to correct for this bias would require knowledge about the expected distribution of amplitude spectra, which is not yet established.

To gauge the potential importance of such a bias, we investigate the inferred $A_\rho(k_{\rm peak})$ using cuts of 2σ, 3σ, 4σ, and 5σ. We don't find (see Figure 4) clear evidence of a substantial bias in the distribution of $A_\rho(k_{\rm peak})$. The respective weighted means of $A_\rho(k_{\rm peak})$ with their statistical uncertainties (ignoring scatter) are 0.162 ± 0.005, 0.156 ± 0.004, 0.159 ± 0.005, and 0.159 ± 0.005, thus revealing no significant tension.

While $A_\rho(k_{\rm peak})$ appears to not suffer a substantial bias, we may also be concerned with the inferred turbulent velocity. Again, we do not see evidence for a clear bias from the 2σ cut (see again Figure 4), where the weighted means are 0.57, 0.57, 0.59, and 0.59 for the respective threshold cuts of 2σ, 3σ, 4σ, and 5σ. Across the thresholds, we can thus find an average turbulent velocity $\mathcal{M}_\rho \sim 0.6$. Additionally, the bottom panel

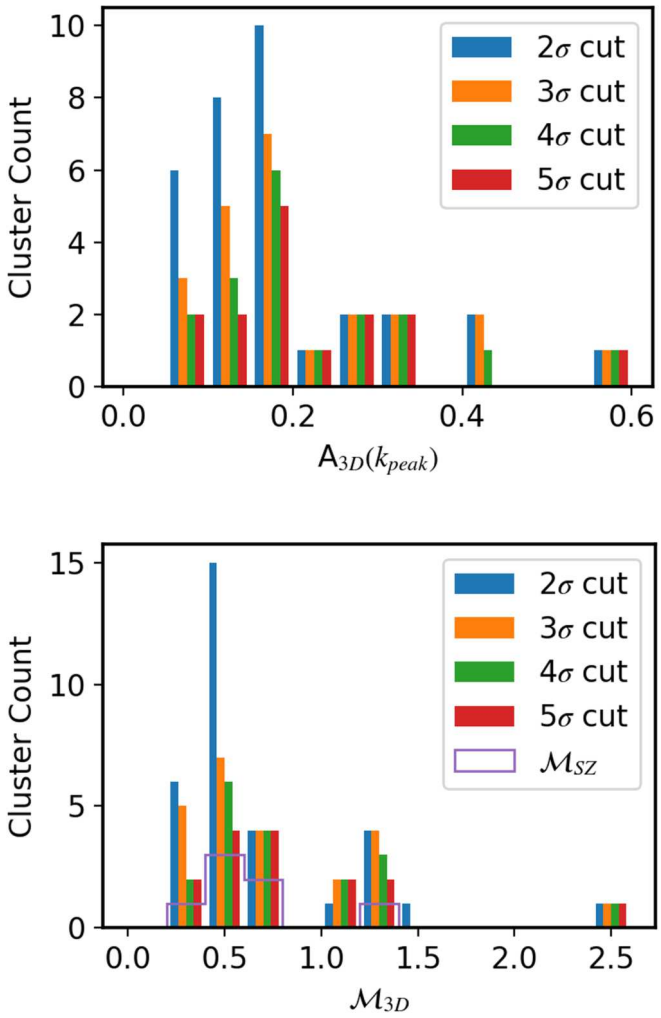

Figure 4. Within Ring 1, distributions of $A_\rho(k_{\rm peak})$ and distributions of Mach numbers, $\mathcal{M}_\rho$, for different significance thresholds on A_ρ and $\mathcal{M}_P$ with A_P significance greater than 1.5σ. For clarity, the blue bars indicate the number of clusters for which we infer a given peak of A_ρ or a given $\mathcal{M}_\rho$ when considering only nodes of amplitude spectra for which $A_\rho > 2\sigma_{A_\rho}$.

of Figure 4 is suggestive of an underlying bimodal distribution, where the two populations are separated at the supersonic transition. Using the dip test from J. A. Hartigan & P. M. Hartigan (1985) on our distribution of Mach numbers, we find dip values less than 0.07 across the threshold cuts, which correspond to probabilities, p, of a unimodal distribution $0.48 < p < 0.84$. For the distribution of $A_{\rm 3D}$ peaks (across the cuts) we find $p > 0.95$. If the distributions are indeed unimodal, they are positively skewed, where the moment of skewness (across all significance cuts) for $A_{\rm 3D}$ peaks is $\geqslant 1.3$, while for $\mathcal{M}_{\rm 3D}$ the values are $\geqslant 1.6$.

To add to these tests, we also investigate a Gaussian mixture and use the changes in the Bayesian information criterion (BIC) between the case of two Gaussians ($\rm BIC_2$) and the case of one Gaussian ($\rm BIC_1$), such that $\Delta{\rm BIC} = {\rm BIC_2} - {\rm BIC_1}$. For the distribution of $A_{\rm 3D}$ peaks, we find $\Delta{\rm BIC} = -14.0$, -5.0, -0.9, and 1.6 for the respective threshold cuts of 2σ, 3σ, 4σ, and 5σ. The analogous values for the $\mathcal{M}_{\rm 3D}$ distributions are $\Delta{\rm BIC} = -18.2$, -6.9, -4.4, and -10.9. R. E. Kass & A. E. Raftery (1995) indicate that $\Delta{\rm BIC} < -6$ provides strong evidence that, in this case, the underlying distribution is best described by two Gaussians rather than a single Gaussian.

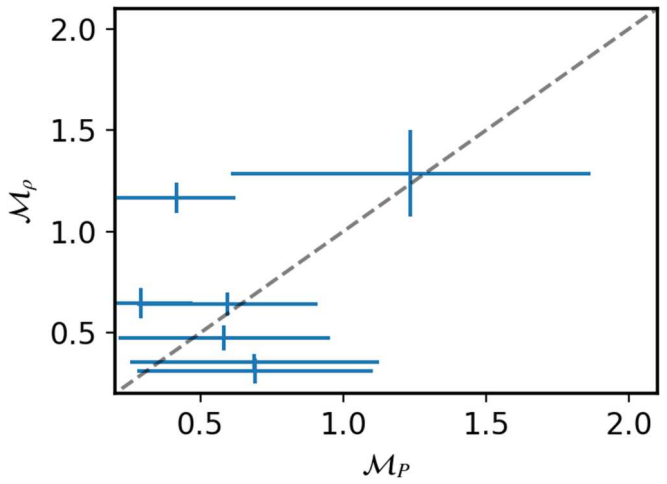

Figure 5. Comparison of $\mathcal{M}_{3D}$ as derived from SZ (pressure) or X-ray (density) fluctuations. The dashed line shows unitary equivalence.

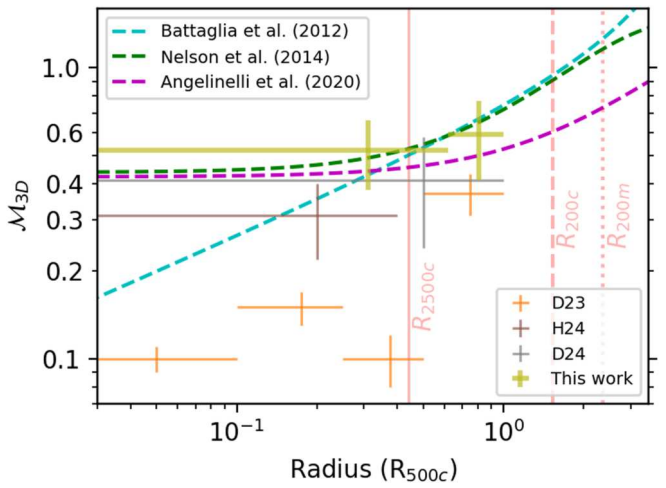

Figure 6. Radial profiles of Mach numbers from various simulations (dashed curves) and observational constraints on Mach numbers as points with uncertainties (in $\mathcal{M}_{3D}$); the radial "error bar" denotes the extent of the radial bin. Observational points identified as D23, H24, and D24 refer to S. Dupourqué et al. (2023), A. Heinrich et al. (2024), and S. Dupourqué et al. (2024), respectively. Points from this work correspond to those in which gas motions have been restricted to subsonic velocities.

Thus, while the dip test suggests a unimodal distribution (as in there is not a robust trough in the distribution), we can confirm that any such unimodal distribution is not well described by a single Gaussian.

We also consider the weighted means if we trim the clusters with supersonic Mach numbers. Doing so, we find weighted means (of the Mach numbers) of 0.52, 0.50, 0.52, and 0.52 for the respective σ cuts. The respective statistical uncertainties of these values are 0.019, 0.016, 0.017, and 0.018, indicating no substantial bias. Such statistical uncertainties ignore intrinsic scatter, which is between 0.12 and 0.14 in all four cases. The median subsonic $\mathcal{M}_\rho$ values for the respective σ cuts are 0.52, 0.50, 0.55, and 0.56. In the case of the 2σ cut, there are 25 clusters with inferred turbulent velocities that are subsonic. When restricting velocities to those that are subsonic, across the thresholds, we find an average $\mathcal{M}_\rho \sim 0.5$. In the following section we discuss the interpretation of supersonic Mach numbers and identify the individual clusters in which we infer supersonic velocities.

For the seven clusters that have SZ constraints (above 1.5σ in Ring 1), we compare the SZ-inferred turbulent velocities to those from X-rays, i.e., we compare the inferences from pressure and density fluctuations, in Figure 5. We find general agreement and note that the point with $\mathcal{M}_\rho > 1$ and $\mathcal{M}_P < 0.5$ corresponds to SPT-CLJ0014-3022 (or A2744). Notwithstanding considerations of masking substructure (see Appendix B), this indicates that the infalling group has not contributed to substantial pressure fluctuations.

4. Discussion

In the previous section we found an average turbulent velocity within Ring 1 ($R < 0.62R_{500}$) that corresponds to $\mathcal{M}_\rho \sim 0.6$ when including all clusters across the considered significance cuts in the amplitude spectrum of density fluctuations. This average becomes $\mathcal{M}_\rho \sim 0.5$ when confining attention to the subset of clusters that also have inferred $\mathcal{M}_\rho < 1$.

Given that turbulence with $\mathcal{M}_{3D} > 1$ is largely not expected within R_{500}, let alone within $0.62R_{500}$, and that the clusters for which we infer $\mathcal{M}_\rho > 1$ have either known merger shocks or morphologies suggestive of mergers (see Section 4.2), we consider that the inferred Mach numbers should not be interpreted as arising solely from turbulence. We discuss this more in the following subsection.

Previous studies of surface brightness fluctuations across samples of similar sizes have tended to find relatively lower 3D Mach numbers than the $\mathcal{M}_\rho = 0.52 \pm 0.14$ found in this work (using clusters with subsonic inferred turbulent velocities and $\xi > 2$; see Section 3.3). For example, F. Hofmann et al. (2016) find an average $\mathcal{M}_\rho \approx 0.3$ with a large 50% scatter in a sample of 33 Chandra clusters. Across the 12 clusters in the small X-COP sample, S. Dupourqué et al. (2023) found $\mathcal{M}_\rho = 0.37 \pm 0.06$ within $0.5R_{500} < r < R_{500}$. Investigating a sample of 80 clusters with Chandra data, A. Heinrich et al. (2024) found $\mathcal{M}_\rho = 0.31 \pm 0.09$ in the region within $0.4R_{500}$. Using 64 (of the 82) clusters in the CHEX-MATE sample, S. Dupourqué et al. (2024) find an average turbulent velocity of $\mathcal{M}_\rho = 0.41 \pm 0.17$ within R_{500}. In 28 of the CHEX-MATE clusters, L. Lovisari et al. (2024) find 17% temperature fluctuations and infer $\mathcal{M}_{3D} = 0.37^{+0.16}_{-0.09}$.

While sample selection may translate into differences in inferred turbulent velocities, neither our sample nor those in other works can be strictly described as SZ- or X-ray-selected. Our treatments of masking substructure or excluding merging systems are also heterogeneous. We investigate differences in sample distributions in Appendix A.

To better understand/test the Mach numbers, we compare them to predictions from cosmological hydrodynamical simulations. N. Battaglia et al. (2012, hereafter B12), K. Nelson et al. (2014, N14), and M. Angelinelli et al. (2020, A20) have investigated nonthermal pressure profiles, P_{NT}, due to random or kinetic motions; A20 provide an explicit separation for the pressure due to strictly turbulent motions. In particular, these works provide parametric forms for $\alpha_{NT} = P_{NT}/(P_{NT} + P_{th})$, where P_{th} is the thermal pressure. For turbulent motions, $P_{turb}/P_{th} = (\gamma/3)\mathcal{M}^2_{3D}$. Thus, where P_{NT} is taken to be, implicitly or explicitly, P_{turb}, one can infer $\mathcal{M}_{3D}$.

Figure 6 shows Mach profiles derived from the nonthermal pressure profiles presented by B12, N14, and A20, where we

take the profile explicitly determined for turbulence from A20. From these profiles we further calculate that within $0.62R_{500}$, the expected $\mathcal{M}_{3D}$ values are 0.49, 0.52, and 0.45 for B12, N14, and A20, respectively. Within Ring 2 ($0.62R_{500} < r < R_{500}$) those respective Mach numbers are 0.68, 0.66, and 0.50. We note that the simulations themselves find a scatter of $\gtrsim$10% in the α_{NT} profiles.

Aside from differences in cluster samples and analytic approaches among S. Dupourqué et al. (2023, 2024), A. Heinrich et al. (2024), and this work, there are differences in the scaling between density fluctuations and inferred Mach numbers that are potentially relevant. While some theoretical agreement has been found between the relations presented by M. Gaspari & E. Churazov (2013), M. Gaspari et al. (2014b), and I. Zhuravleva et al. (2014, 2023), it will be important to establish a robust, empirical relation between density (and pressure) fluctuations and turbulent velocities inferred from high-resolution X-ray spectroscopy, e.g., with the ongoing XRISM mission.

4.1. Nonthermal Pressure Support and Hydrostatic Mass Bias

Our inferred average turbulent Mach number, $\mathcal{M}_\rho = 0.52 \pm 0.14$, in Ring 1 is thus in excellent agreement with what is expected from simulation. This turbulent Mach number corresponds to a nonthermal pressure fraction $\alpha_{NT} = 0.13 \pm 0.06$. This value does not necessarily reflect the hydrostatic mass bias, which is instead given by

$$b_{\mathcal{M}} = \frac{-\gamma \mathcal{M}_{3D}^2}{3} \frac{d \ln P_{NT}}{d \ln P_{th}} \left(1 + \frac{\gamma \mathcal{M}_{3D}^2}{3} \frac{d \ln P_{NT}}{d \ln P_{th}}\right)^{-1} \quad (6)$$

(R. Khatri & M. Gaspari 2016; C. E. Romero et al. 2024). That is, $\alpha_{NT} = -b_{\mathcal{M}}$ only when $d \ln P_{NT}/d \ln P_{th} = 1$. Considering that

$$\frac{d \ln P_{NT}}{d \ln P_{th}} = 1 + 2 \frac{d \ln \mathcal{M}_{3D}/d \ln r}{d \ln P_{th}/d \ln r}, \quad (7)$$

we see that $d \ln P_{NT}/d \ln P_{th} = 1$ when the turbulent Mach number is constant with radius. We expect that $\mathcal{M}_{3D}$ should, in general, increase with radius (as in Figure 6) and consequently we expect that $-b_{\mathcal{M}} < \alpha_{NT}$.

From the above, we can say that we expect the average hydrostatic mass bias within Ring 1 to be less than 0.13 (for those clusters with inferred subsonic turbulence). Given that masses are generally not provided at $0.62R_{500}$, the hydrostatic mass bias at R_{500} is of more interest. However, our constraints from Ring 2 are poorer and we discuss these in detail in Appendix D. From the few (four) clusters that have sufficient constraints (at least 2σ significance in $A_{\rho,2}$) and yield subsonic turbulent velocities, we find $\mathcal{M}_{\rho,2} = 0.59 \pm 0.18$ with corresponding $\alpha_{NT} = 0.16 \pm 0.08$. We can take this to define an upper limit of the hydrostatic mass bias: $-b_{\mathcal{M}} < 0.16 \pm 0.08$. Such an interpretation is consistent with the expected hydrostatic mass bias values between 0.1 and 0.3 (e.g., C. E. Romero et al. 2024, and references therein); though we note again that the sample size is small (four clusters) and the constraints are of limited quality. This motivates our later discussion in Section 4.3.

4.2. Inferred Supersonic Velocities

The clusters for which $\mathcal{M}_\rho > 1$ are SPT-CLJ0354-5904, SPT-CLJ0658-5556, SPT-CLJ2017-6258, SPT-CLJ2056-5459, SPT-CLJ0304-4401, SPT-CLJ2032-5627, and SPT-CLJ0014-3022. Of these, SPT-CLJ0354-5904, SPT-CLJ2017-6258, and SPT-CLJ2056-5459 show asymmetries or potential substructure in the XMM images that is suggestive of disturbance. Dynamical parameters from Z. S. Yuan et al. (2022) for these three clusters corroborate this. For example, all three of these clusters have profile parameters, $\kappa > 2$, and of the 32 clusters with sufficient constraints, these three are among the top five clusters with respect to highest values of κ. However, our substructure algorithm did not identify any substructure to mask, in part due to the modest photon counts in those images. SPT-CLJ0658-5556 (the Bullet cluster), SPT-CLJ0014-3022 (A2744), SPT-CLJ0304-4401, and SPT-CLJ2032-5627 are known mergers (M. Markevitch et al. 2002; J. C. Kempner & L. P. David 2004; S. W. Duchesne et al. 2021; R. Raja et al. 2021).

In the known mergers, we find that known or plausible shocks are within the same regions in which we infer $\mathcal{M}_\rho > 1$, consistent with our findings (C. E. Romero et al. 2024). Our analysis has assumed that density and pressure fluctuations, A_{3D}, scale linearly with the Mach number, which should hold for distributed turbulence (Section 1). However, the inferred density and pressure fluctuations represent a volume-weighted average that can be accentuated to superlinear levels by the influence of local shock(s), which are inherently supersonic. We note that by superlinear fluctuations we mean that $A_{3D}(k_{peak}) \propto \mathcal{M}_{3D}^x$ with $x > 1$. Such behavior due to shocks within a region could explain the skewed, if not bimodal, distribution of our inferred Mach numbers (in Figure 4). From another perspective, someone could select a target cluster from superlinear fluctuations, and then investigate the (likely) presence of shocks with deeper observations.

A more detailed interpretation of these supersonic velocities is likely to be complicated by several factors. As is often the case, the inclination angle of features, in this case shocks or a sloshing core, will impact the surface brightness signature. The current method of inferring gas velocities is developed in the context of turbulent motions and does not explicitly account for such substructure and thus different inclination angles. As such, we acknowledge that our inferred volume-averaged gas velocities have additional (unaccounted) systematic uncertainties. Secondarily, there is the matter of masking, which has evaded a widely accepted identification strategy (e.g., I. Zhuravleva et al. 2015; S. Dupourqué et al. 2023, and this work). The Bullet cluster and A2744 provide some insight here, insofar as it is clear that our masking algorithm has masked the cooler gas behind the shocks in those two clusters, and *not* the shocks themselves.

4.3. Toward More Sensitive Measurements

This project aimed to constrain both pressure and density fluctuations, ideally out to R_{500}, over a sample of galaxy clusters with both sensitive X-ray and SZ data. We find that it is already difficult to place tight constraints on these fluctuations within $0.62R_{500}$. On the SZ side, constraints on pressure fluctuations are at best 2σ. The ongoing SPT-3G survey (B. A. Benson et al. 2014) is expected to reach a final depth 10 times that of the SPT-SZ survey, and

correspondingly, we should expect the uncertainties in amplitude spectra to improve by a factor of 10 except for the nodes at the largest scales, which may become dominated by cosmic variance (e.g., C. E. Romero 2024). This will allow some insight into pressure fluctuations, but the constraints across spatial scales will still be limited, due to the expected power spectrum of pressure fluctuations and the angular resolution achieved by SPT-3G.

With respect to the dependence of the SNR on the angular frequency, k, we can take a simple case where the statistical noise in y or S maps has a flat power spectrum. In this case, the uncertainty in the measurements of surface brightness fluctuations will scale as k^{-1} (P. Arévalo et al. 2012; C. E. Romero 2024). At scales smaller than the injection scale, the power spectrum will have a logarithmic slope steeper than -3, where at some frequency beyond $k_{\rm inj}$, a logarithmic slope of $11/3$ is predicted for Kolmogorov turbulence. Therefore, we can consider that the SNR is declining at a rate steeper than k^{-2} beyond the injection scale.

While the resolution of XMM-Newton has a nontrivial impact on measurements of density fluctuations, we see that, in fact, constraints at the smallest scales tend to still be limited by overall sensitivity owing to the scaling of SNR with k. Consider that we do achieve $>3\sigma$ constraints at spatial scales corresponding to $\sim 0.4R_{500}$, which appears to be a plausible injection scale (e.g., M. Gaspari et al. 2014b). Suppose a cluster has a constraint of 3σ at $0.4R_{500}$ and we wish to obtain 3σ constraints at $0.1R_{500}$; we would need to improve the SNR by at least 16 times, which will require a factor of $16^2 = 256$ more time.

When we consider how the required time scales, this suggests requirements of clean exposure time with XMM-Newton in excess of 1 Ms (per cluster) to achieve 3σ constraints at $0.1R_{500}$, in Ring 1 across our sample. From the constraints we do have in Ring 2, we find that the requirements for clean exposure time exceed 10 Ms (per cluster; sometimes exceeding 100 Ms) for the same target constraint. It is clear that such constraints must be tasked to future facilities.

We would be remiss to not mention constraints to come from high-resolution spectroscopy, especially from XRISM (XRISM Science Team 2020) and the proposed Athena (D. Barret et al. 2020; M. Cruise et al. 2025) telescope. These will clearly play an important role in constraining turbulent motions in clusters. While there has not been a study comparing required observing times across spectroscopic instruments, nor a dedicated study comparing constraints from spectroscopy to those from surface brightness fluctuations, C. E. Romero (2024) found that, for similar collecting areas, constraints from surface brightness fluctuations can be obtained with exposures that are one to two orders of magnitude shorter than those from spectroscopy.[16]

5. Conclusions

Expanding on our previous pilot investigations of surface brightness fluctuations jointly in the SZ and in X-rays (R. Khatri & M. Gaspari 2016; C. E. Romero et al. 2023, 2024), we analyzed here, for the first time, a large sample of 60 clusters using both SPT and XMM-Newton data. We thus derived constraints on density and pressure fluctuations within $\sim 0.6R_{500}$ for 32 and 7 clusters, respectively, and converted them to 3D Mach numbers through the linear relation with peak amplitude (M. Gaspari & E. Churazov 2013). We were able to derive constraints on density fluctuations out to R_{500} for 15 clusters, but the interpretation of those fluctuations is unclear. We thus focus on the interpretation of fluctuations within $0.62R_{500}$; our main results tied to this region are as follows.

1. We find the mean Mach number to be $\mathcal{M}_\rho = 0.52\pm 0.14$ for the 25 clusters that we consider to be dominated by turbulence and consistent with expectations from simulations (N. Battaglia et al. 2012; K. Nelson et al. 2014; M. Angelinelli et al. 2020).
2. Clusters with supersonic $\mathcal{M}_\rho > 1$ are either known to be or plausibly are undergoing a merger, and thus likely are shock-dominated systems.
3. For clusters with constraints on both density and pressure fluctuations, the inferred velocities are generally in agreement (except in A2744).
4. We find mild correlations between the spectral amplitude/Mach number and the cluster dynamical parameters that are typically used in the literature.
5. Conversely, we find no significant correlation between the spectral amplitude/Mach number and either cluster mass or redshift, which is consistent with other observational and theoretical studies.

In order to obtain robust results out to R_{500}, as well as tracing the full turbulent cascade, deeper observations are required. Some meaningful improvements are in progress, with SPT-3G, and can be obtained with deep XMM-Newton observations. However, for the less massive and higher-redshift clusters, robust constraints must come from a future generation of instruments, in both X-ray and SZ bands.

Acknowledgments

The authors would like to thank the anonymous referee for comments that have improved this work.

C.R. acknowledges support from NASA ADAP grant 80NSSC19K0574 and Chandra grant G08-19117X. M.G. acknowledges funding support from the ERC Consolidator grant BlackHoleWeather (101086804). R.K. acknowledges support from the Smithsonian Institution, the Chandra High Resolution Camera Project through NASA contract NAS8-03060, and NASA grants 80NSSC19K0116, GO1-22132X, and GO9-20109X. P.N. was supported by NASA contract NAS8-03060. C.L.R. acknowledges support from the Australian Research Council's Discovery Project scheme (No. DP200101068). Y.S. acknowledges support from Chandra grants GO1-22126X and GO2-23120X. E.B. acknowledges financial support from the ERC Consolidator grant DarkQuest (101002585). W.F. acknowledges support from the Smithsonian Institution, the Chandra High Resolution Camera Project through NASA contract NAS8-0306, NASA grant 80NSSC19K0116 and Chandra grant GO1-22132X.

The South Pole Telescope program is supported by the National Science Foundation (NSF) through awards OPP-1852617 and OPP-2332483. Partial support is also provided by the Kavli Institute of Cosmological Physics at the University of Chicago. Argonne National Laboratory's work was supported by the U.S. Department of Energy, Office of High

[16] This comparison was made between the results of C. E. Romero (2024) and those of S. Beaumont et al. (2024). As the differences in the methodologies are not trivial, a more judicious comparison between constraints from surface brightness fluctuations and high-resolution spectroscopy is warranted.

Energy Physics, under contract DE-AC02-06CH11357. Work at Fermi National Accelerator Laboratory, a DOE-OS, HEP User Facility managed by the Fermi Research Alliance, LLC, was supported under Contract No. DE-AC02-07CH11359.

Facilities: SPT, XMM.

Software: astropy (Astropy Collaboration et al. 2013, 2022; The Astropy Collaboration 2018), emcee (D. Foreman-Mackey et al. 2013), pyproffit (D. Eckert et al. 2017), ESAS (S. L. Snowden et al. 2008).

Appendix A
Cluster Properties

Tables 3 and 4 list various observational properties of the clusters. Clusters with density fluctuations in Ring 1, $A_{\rho,1}$, with at least one node of SNR $\xi > 2$ are listed in Table 3 along with key properties of $A_{\rho,1}$. Conversely, clusters that do not satisfy the SNR threshold are listed in Table 4. SPT-CLJ2344-4243 (Phoenix cluster), SPT-CLJ0637-4829, SPT-CLJ0330-5228, and SPT-CLJ2332-5358 are omitted from these tables. In the

Table 3
Cluster Characteristics, Observational Properties, and Inferred Values

Cluster	z[a]	θ_{500}	$\xi_{\rm SPT}$[a]	M_{500}[b] (10^{14}	Obs. ID	Exposures (ks)	Counts	$k_{\rm peak}$	$A_{\rho,1}(k_{\rm peak})$	$\mathcal{M}_{\rho,1}$	$\xi_{A_{\rho,1}}$
(SPT-CLJ)		(arcmin)		$M_\odot$)		MOS1;MOS2;PN	MOS1;MOS2;PN	(R_{500}^{-1})			(max)
2248-4431	0.35	4.96	42.36	13.05	0504630101	25.70;26.60;21.90	14127;14012;36984	3.97	0.10 ± 0.05	0.44 ± 0.22	12.09
0658-5556	0.29	5.71	39.05	12.70	0112980201	22.20;22.20;18.00	12730;12380;31034	4.57	0.28 ± 0.05	1.29 ± 0.21	15.91
0549-6205	0.37	4.30	25.81	9.66	0656201301	13.40;13.10;9.90	4223;3908;10405	3.44	0.12 ± 0.05	0.53 ± 0.22	7.78
	…	…	…	…	0827050701	39.50;39.70;37.90	12057;11211;37560	…	…	…	
0232-4421	0.28	5.33	23.96	9.45	0042340301	11.60;12.10;6.80	4414;4757;9652	2.63	0.16 ± 0.02	0.65 ± 0.08	9.51
	…	…	…	…	0827350201	24.60;25.70;18.00	9403;9393;26991	…	…	…	
0638-5358	0.23	6.26	22.69	9.42	0650860101	24.60;31.70;7.60	11177;14200;13067	1.71	0.18 ± 0.02	0.64 ± 0.06	11.49
0438-5419	0.42	3.77	22.88	8.68	0656201601	18.00;18.00;13.50	3002;2907;7331	3.01	0.14 ± 0.05	0.57 ± 0.21	9.21
	…	…	…	…	0827360501	37.80;40.30;33.60	6230;6386;18737	…	…	…	
2031-4037	0.34	4.31	17.52	7.95	0690170501	2.50;2.50;0.80	352;368;432	1.00	0.08 ± 0.04	0.26 ± 0.11	2.30
	…	…	…	…	0690170701	10.30;10.10;8.60	1565;1522;4800	…	…	…	
2106-5844	1.13	1.80	22.22	7.14	0744400101	41.50;46.30;19.30	1146;1055;1901	1.00	0.22 ± 0.04	0.70 ± 0.12	5.75
	…	…	…	…	0763670301	26.80;27.70;18.40	688;746;1729	…	…	…	
2337-5942	0.77	2.28	20.35	7.05	0604010201	18.20;19.70;10.20	740;737;1462	1.00	0.13 ± 0.05	0.42 ± 0.17	2.49
0304-4401	0.46	3.27	15.69	6.98	0700182201	16.90;16.80;13.00	1570;1457;3926	2.62	0.34 ± 0.05	1.37 ± 0.19	10.06
2023-5535	0.23	5.53	13.63	6.49	0841951701	13.90;14.00;11.40	2338;2402;6837	1.00	0.19 ± 0.02	0.59 ± 0.06	9.75
0243-4833	0.50	2.97	13.90	6.26	0672090501	10.40;10.20;5.30	772;772;1651	1.00	0.09 ± 0.03	0.29 ± 0.09	3.23
	…	…	…	…	0723780801	12.70;11.60;3.70	987;980;1063	…	…	…	
2138-6008	0.32	4.14	12.64	6.10	0674490201	13.10;14.40;9.80	1260;1340;2822	1.00	0.07 ± 0.03	0.22 ± 0.08	2.70
0114-4123	0.38	3.57	11.43	5.86	0724770901	12.40;12.80;7.40	926;973;2034	1.00	0.07 ± 0.03	0.21 ± 0.08	2.63
0014-3022	0.12	9.20	18.29	5.43	0042340101	13.90;14.20;10.90	3337;3499;7740	14.40	0.28 ± 0.13	1.70 ± 0.79	19.47
	…	…	…	…	0743850101	96.50;96.60;82.80	22015;21716;58130	…	…	…	
0559-5249	0.61	2.39	10.64	5.03	0604010301	18.30;18.20;13.50	415;391;1059	1.00	0.18 ± 0.04	0.57 ± 0.14	4.02
2341-5119	1.00	1.71	12.49	4.94	0744400401	74.30;84.20;47.30	1189;1294;2869	1.00	0.12 ± 0.03	0.39 ± 0.10	3.87
	…	…	…	…	0763670201	31.10;35.20;16.10	503;527;990	…	…	…	
2146-4633	0.93	1.79	9.67	4.89	0744400501	94.10;97.90;70.50	1209;1148;3466	1.43	0.16 ± 0.05	0.56 ± 0.16	3.73
	…	…	…	…	0744401301	71.50;75.30;44.50	883;917;2277	…	…	…	
0240-5946	0.40	3.22	8.84	4.85	0674490101	14.30;14.20;7.90	779;759;1381	1.00	0.17 ± 0.06	0.54 ± 0.20	2.73
2032-5627	0.28	4.24	8.61	4.77	0674490401	25.10;25.80;19.30	3162;3538;8248	3.39	0.56 ± 0.04	2.40 ± 0.17	14.62
2124-6124	0.44	2.94	8.50	4.60	0674490701	14.10;14.70;7.90	434;487;862	1.00	0.14 ± 0.07	0.46 ± 0.22	2.06
0225-4155	0.22	5.02	6.92	4.33	0692933401	12.50;12.20;10.90	3862;3643;11651	4.01	0.16 ± 0.01	0.74 ± 0.05	17.02
	…	…	…	…	0803550101	64.20;68.40;50.70	19341;21865;42391	…	…	…	
2017-6258	0.53	2.46	6.32	4.03	0674491501	25.90;25.80;20.80	328;273;833	1.00	0.41 ± 0.11	1.30 ± 0.34	3.80
0344-5452	1.00	1.58	7.98	3.89	0675010701	49.50;49.70;43.00	303;248;1044	1.00	0.16 ± 0.08	0.51 ± 0.24	2.12
0254-5857	0.44	2.78	14.13	3.86	0656200301	11.90;13.30;6.80	1081;1368;2116	1.49	0.15 ± 0.01	0.53 ± 0.05	10.84
	…	…	…	…	0674380301	45.90;47.20;38.90	4493;4383;12464	…	…	…	
0354-5904	0.41	2.92	6.42	3.83	0724770501	14.80;16.30;9.10	333;554;968	1.00	0.33 ± 0.05	1.06 ± 0.17	6.27
0317-5935	0.47	2.61	6.26	3.73	0674490501	8.10;10.90;1.90	232;270;204	1.00	0.13 ± 0.05	0.41 ± 0.17	2.44
	…	…	…	…	0724770401	15.00;15.10;7.30	567;489;921	…	…	…	
0233-5819	0.66	2.05	6.55	3.70	0675010601	49.70;50.90;38.30	754;736;2183	1.00	0.10 ± 0.03	0.31 ± 0.11	2.96
0403-5719	0.46	2.60	5.86	3.52	0674491201	18.60;20.00;10.10	994;1104;1893	1.44	0.15 ± 0.05	0.52 ± 0.18	3.35
0522-4818	0.29	3.67	4.82	3.37	0303820101	11.60;15.30;3.10	863;957;680	1.00	0.14 ± 0.03	0.45 ± 0.11	4.19
2056-5459	0.72	1.87	6.07	3.36	0675010901	40.70;39.80;36.00	371;396;1167	1.00	0.42 ± 0.10	1.33 ± 0.32	4.14
2011-5725	0.28	3.77	5.34	3.35	0744390401	17.20;17.70;10.50	739;799;1036	1.74	0.16 ± 0.05	0.59 ± 0.20	5.18

Notes. Properties of clusters for which at least one node in $A_{\rho,1}$ has an SNR of $\xi > 2$.

[a] Values taken from S. Bocquet et al. (2019) and for SPT-CLJ0014-3022 from T. Plagge et al. (2010). $\xi_{\rm SPT}$ refers to the detection significance of the cluster from SPT data (L. E. Bleem et al. 2015).

[b] Values taken from E. Bulbul et al. (2019). θ_{500} is inferred from M_{500} and our assumed cosmology. $\xi_{\rho,1}$ refers to the maximum significance of nodes within the amplitude spectrum $A_{\rho,1}$.

Table 4
Cluster Characteristics and Observational Properties for Nondetections

Cluster	z[a]	θ_{500} (arcmin)	ξ^{a}_{SPT}	M^{b}_{500} ($10^{14}\ M_{\odot}$)	Obs. ID	Exposures (ks) MOS1;MOS2;PN	Counts MOS1;MOS2;PN
SPT-CLJ0615-5746	0.97	2.11	26.42	8.69	0658200101	12.70;13.40;5.20	641;643;663
SPT-CLJ0234-5831	0.42	3.45	14.66	6.70	0674491001	12.70;13.80;9.10	1485;1580;3558
SPT-CLJ2131-4019	0.45	3.21	12.51	6.25	0724770601	12.70;12.90;6.20	1288;1395;2417
SPT-CLJ0417-4748	0.58	2.66	14.24	6.22	0700182401	22.10;23.80;15.30	1646;1754;3981
SPT-CLJ0516-5430	0.29	4.44	12.41	5.96	0042340701	5.00;5.00;0.80	1006;1096;482
					0205330301	10.40;10.70;8.10	2166;2210;5323
					0692934301	27.50;27.40;23.60	5452;5513;14735
SPT-CLJ2145-5644	0.48	2.98	12.60	5.82	0674491301	10.30;10.70;6.40	619;666;1221
SPT-CLJ0510-4519	0.20	5.97	9.50	5.73	0692933001	13.00;13.10;11.10	4007;3975;11859
SPT-CLJ0205-5829	1.32	1.39	10.40	4.37	0675010101	57.00;57.90;46.70	472;412;1208
					0803050201	10.50;12.40;6.00	82;74;150
SPT-CLJ2130-6458	0.31	3.78	7.63	4.33	0692900101	6.30;8.20;4.10	403;489;938
SPT-CLJ0254-6051	0.44	3.31	6.55	6.52	0692900201	16.20;15.70;12.20	316;334;1027
SPT-CLJ0217-5245	0.34	3.43	6.46	4.01	0652951401	9.30;14.70;3.80	332;470;448
SPT-CLJ2022-6323	0.38	3.09	6.51	3.80	0674490601	14.70;14.40;5.80	290;201;373
SPT-CLJ2200-6245[c]	0.39	3.02	0.00	3.79	0674490801	9.60;10.70;6.20	180;140;343
					0724771001	Not used	Not used
SPT-CLJ0343-5518	0.55	2.29	6.01	3.52	0724770801	18.10;18.00;11.80	252;265;635
SPT-CLJ0230-6028	0.68	1.95	6.01	3.43	0675010401	19.50;25.40;11.20	295;412;705
SPT-CLJ2030-5638	0.39	2.90	5.50	3.35	0724770201	21.10;21.10;17.10	391;398;1133
SPT-CLJ2040-4451	1.48	1.19	6.72	3.31	0723290101	76.30;76.10;72.90	280;282;1019
SPT-CLJ0406-5455	0.74	1.82	5.91	3.28	0675010501	54.20;56.10;40.00	426;354;1218
SPT-CLJ2136-6307	0.93	1.56	6.24	3.24	0675010301	57.30;60.80;50.30	429;417;1164
SPT-CLJ2040-5725	0.93	1.56	6.24	3.23	0675010201	75.70;77.30;68.40	783;600;2113
SPT-CLJ0231-5403	0.59	2.10	5.22	3.18	0204530101	17.30;22.00;4.50	195;320;146
SPT-CLJ0257-5732	0.43	2.64	5.04	3.15	0674491101	27.60;28.10;23.10	180;125;530
SPT-CLJ0611-5938	0.39	2.84	4.74	3.13	0658201101	13.10;13.40;6.30	367;302;616
SPT-CLJ2109-4626	0.97	1.43	4.65[a]	[b]2.68[c]	0694380101	53.10;56.10;43.30	224;159;593

Notes. Properties of clusters for which amplitude spectra were produced but for which the SNR threshold $\xi > 2$ was not met.
[a] Values taken from S. Bocquet et al. (2019) and for SPT-CLJ0014-3022 from T. Plagge et al. (2010). ξ_{SPT} refers to the detection significance of the cluster from SPT data (L. E. Bleem et al. 2015).
[b] Values taken from E. Bulbul et al. (2019). θ_{500} is inferred from M_{500} and our assumed cosmology.
[c] Listed with this moniker by E. Bulbul et al. (2019), it is more commonly found with the moniker SPT-CLJ2159-6244.

case of SPT-CLJ2344-4243, the bright cool core and asymmetries of the XMM-Newton point-spread function present a challenge beyond the scope of this work. The remaining three clusters suffered from complications in ESAS processing.

A.1. Cluster Distribution

Here, we consider how the distribution of the clusters in our SPT-XMM sample compares to its ostensible parent distribution, the clusters in the SPT-SZ catalog. Although we may ultimately care about the distribution in the mass (M_{500})–redshift plane, we describe their distributions against mass and redshift separately here. Namely, Figure 7 shows how our SPT-XMM sample compares to the SPT-SZ sample (redshift and mass values are taken from S. Bocquet et al. 2019), and its subsample used for cosmological results applying the cuts, i.e., $z > 0.25$ and $\xi_{SPT} > 5$, resulting in 343 clusters (e.g., T. de Haan et al. 2016; S. Bocquet et al. 2019).

In addition to Figure 7, we also calculate median redshifts and masses (M_{500}). The median redshifts for the full SPT-SZ sample and its cosmological subsample are 0.55 and 0.59, respectively. The median redshifts of our SPT-XMM sample and the 32 clusters that yielded significant results (amplitude spectra with at least one node of $\xi > 2$) are 0.44 and 0.42, respectively. The median masses of these last two samples are $5.63 \times 10^{14}\ M_{\odot}$ and $5.89 \times 10^{14}\ M_{\odot}$, respectively. The respective median redshifts of the full and cosmological SPT-SZ samples are $4.07 \times 10^{14}\ M_{\odot}$ and $4.40 \times 10^{14}\ M_{\odot}$.

A.2. Comparison of Distributions

Analyzing our cluster distribution in mass and redshift space is appropriate to understand how representative our sample is of a proper SZ-selected sample. However, we also found in Section 3 that density fluctuations (and thus our inferred turbulent velocities) did not correlate with mass (nor other quantities that should also correlate with mass) or redshift. Indeed, this lack of correlation was also seen by S. Dupourqué et al. (2024, hereafter D24). Thus, while we find the median redshifts of the samples of D24 and A. Heinrich et al. (2024, hereafter H24) to be 0.19 and 0.17, respectively, we should not expect this to account for the difference in inferred Mach numbers between those studies, nor relative to our study (when limiting to our clusters with inferred subsonic turbulence, $z_{med} = 0.42$). We do not consider a median mass comparison due to heterogeneous M_{δ} being reported, along with heterogeneous derivations of masses.

Although our sample is not purely SZ-selected, nor are the samples of H24 or D24 purely X-ray-selected, we do, in fact, see differences in the distribution of dynamical parameters

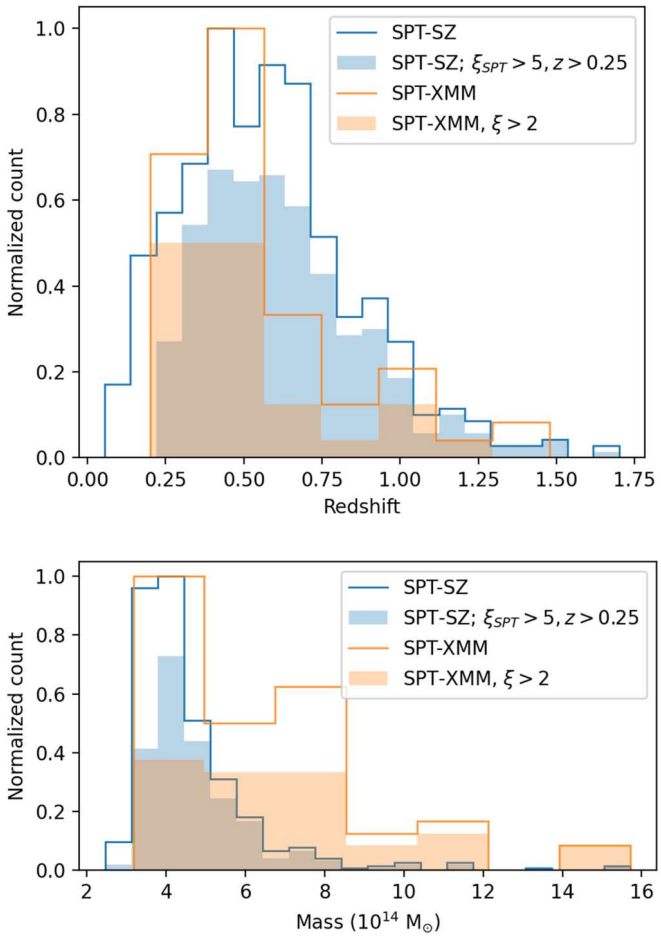

Figure 7. Mass and redshift distributions of our (SPT-XMM) sample and the subset of clusters for which we have significant results ($\xi > 2$). We compare against the SPT-SZ sample and its subset used for cosmological constraints ($\xi_{\rm SPT} > 5$ and $0.25 < z$). Distributions of subsets are normalized relative to their parent samples (retaining the same, respective, binning).

between these samples, as shown in Figure 8. In particular, we utilize the same parameters assessed in Section 3: c, P_3/P_0, α, ω, κ, and δ, which (again) correspond to a concentration index, power ratio, asymmetry factor, peak–centroid offset, profile parameter, and morphology index, respectively. In particular, our sample (even limiting to those clusters for which we infer subsonic turbulent velocities) tends to have more dynamically disturbed clusters than H24 or D24. Indeed, D24 made an explicit effort to omit merging systems (with their selection on the centroid offset parameter), which may be warranted in the hopes of properly tracing turbulence. Conversely, simulations have not selected on this same parameter, so one might expect a difference between simulations on this selection criterion alone.

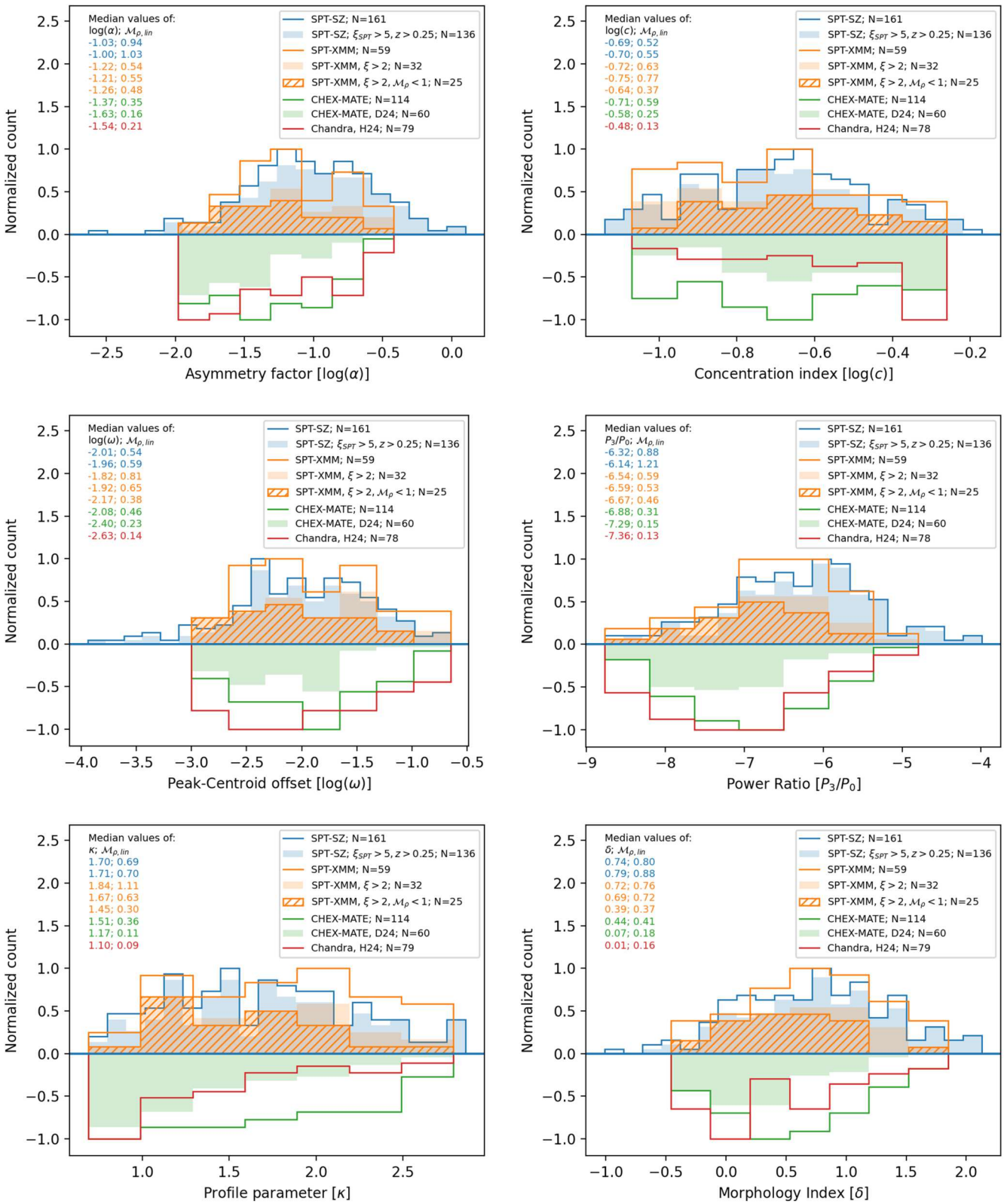

Figure 8. Distributions of the six dynamical parameters presented by Z. S. Yuan et al. (2022) for various samples (sign flipped for some samples to help with visibility). The number of clusters included, N, reflects the fact that Z. S. Yuan et al. (2022) do not necessarily have dynamical parameters for all clusters in considered samples. Distributions of subsets are normalized relative to their parent samples (retaining the same, respective, binning). Text at the upper left of each panel indicates the median values of the dynamical parameter in question along with the median Mach number one would obtain from the linear coefficients presented in Table 2; the ordering (and coloring) matches that in the legend.

Appendix B
Masking Substructure

We employ an algorithm to identify substructure and its extent using net rate images smoothed with three different Gaussian kernels. For each EPIC camera and each energy band, we apply the three smoothing kernels, indexed with k. For each smoothing kernel and within each annulus, indexed with j, of our radial profile we calculate pixel means, $\bar{p}_{j,k}$, and the rms within that annulus (for that smoothing), i.e., $\sigma_{j,k}$. For a normal distribution, and a given number of pixels, we can infer that for some multiplicative factor f of the rms, we will not expect to find any pixels with value $p > \bar{p} + f\sigma$. Within the context of our annuli and smoothings, we flag pixels with $p_{j,k} > \bar{p}_{j,k} + f_j\,\sigma_{j,k}$. A mask could then be produced per smoothing of each EPIC camera.

For a given smoothing, we expect similar substructure to be flagged across the EPIC cameras. However, visual inspection showed that what was masked in one camera may not be masked (or with many fewer pixels masked) in another camera. To ameliorate this, we introduced another factor, per smoothing kernel, g_k such that we flag pixels $p_{j,k} > \bar{p}_{j,k} + g_k f_j\,\sigma_{j,k}$. The values of the adjustments are modest, where $0.5 < g < 2$ yields visual consistency across the cameras. Visual consistency was not rigorously defined, but approximately corresponds to the number of pixels for a given substructure matching within a factor of 2 across all cameras. Initially, a given g_k value that may have produced (visual) consistency for one cluster did not produce (visual)

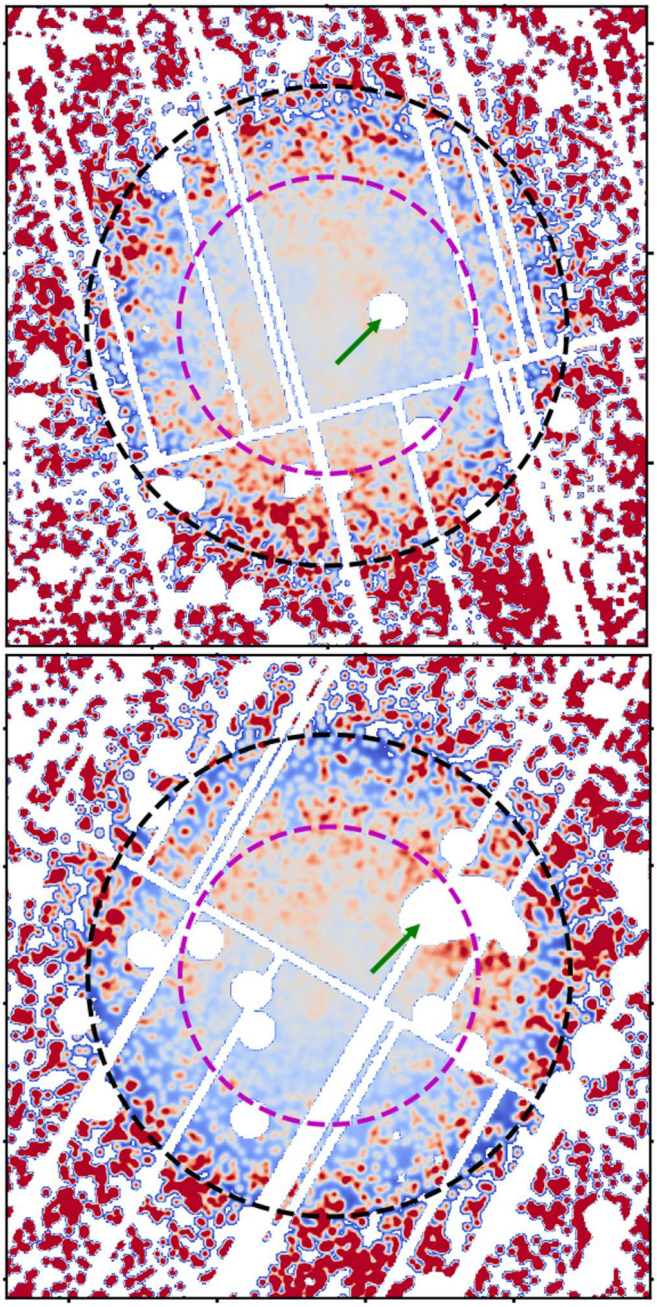

Figure 9. The $\delta S/\bar{S}_{\rm ICM}$ image for SPT-CLJ0658-5556 (top) and SPT-CLJ0014-3022 (bottom) as seen with the pn camera (400–1250 eV). The substructures masked are indicated with green arrows; other masked regions are from point sources and chip gaps.

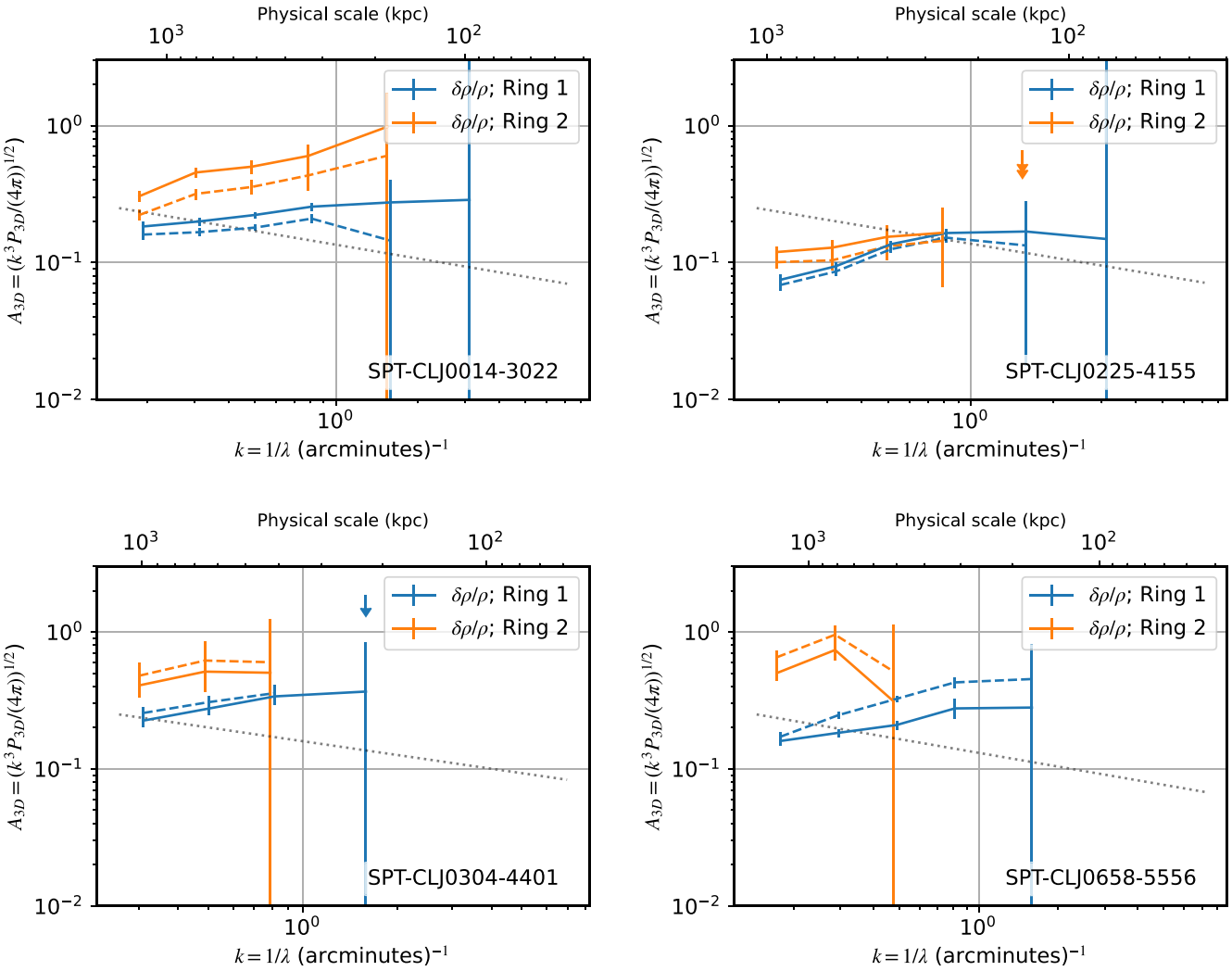

Figure 10. The resultant amplitude spectra, A_ρ, for clusters with substructure masked (solid lines) and unmasked (dashed lines). The clusters are SPT-CLJ0014-3022 (top left), SPT-CLJ0225-4155 (top right), SPT-CLJ0304-4401 (bottom left), and SPT-CLJ0658-5556 (bottom right). Arrows indicate a 3σ upper limit.

consistency for another. After some iteration, we found values of g_k, independent of cluster, that produced consistency. This flagging yielded binary masks per EPIC camera (MOS1, MOS2, and pn) and each energy band (400–1250 eV and 2000–5000 eV). For each cluster, we stacked the binary masks from each EPIC camera and energy band, gently smoothed the stacked mask, and employed another threshold to obtain a merged (binary) mask that closely matched the individual masks.

Figure 9 shows the normalized residuals, $\delta S/\bar{S}_{\rm ICM}$, for SPT-CLJ0658-5556, with the substructure masking algorithm masking solely the Bullet (and not the bow shock). In the case of the Bullet cluster, masking the substructure (the Bullet) reduces the recovered fluctuations as seen in the amplitude spectra (Figure 10). However, for some clusters (e.g., SPT-CLJ0014-3022 and SPT-CLJ0225-4155), the amplitudes can increase. Much as found by C. E. Romero et al. (2024), changes in the surface brightness profile modeling, such as masking, which induce a steeper profile (thus smaller $\bar{S}_{\rm ICM}$ values), can ultimately yield larger fluctuations ($\delta S/\bar{S}_{\rm ICM}$). Another effect is that, for a fixed $P_{\rm 2D}$, the deprojection will produce larger values of $P_{\rm 3D}$, and thus $A_{\rm 3D}$, relative to its counterpart from a surface brightness profile with a shallower slope.

Appendix C
Amplitude Spectra

In Figure 11 we present the amplitude spectra of those clusters for which A_ρ in Ring 1 had at least one node with significance $\xi > 9$. This is an arbitrary choice to showcase a handful of clusters with the best data (especially spectra with three or more nodes of $\xi > 2$). Without clear observations of the spectral cascade, i.e., significant constraints at scales smaller than the observed peaks (with $\xi_{A_\rho} > 2$), we are limited in how well we can infer the injection scales. To the extent that a drop-off at larger scales than the injection scale is expected (e.g., M. Gaspari & E. Churazov 2013), the relatively flat spectra (e.g., that of Ring 1 in SPT-CLJ2248-4431 or SPT-CLJ0014-3022, for which many nodes have $\xi > 5$) suggest multiple injection scales.

This potential has been noted in other works (e.g., S. Dupourqué et al. 2023; C. E. Romero et al. 2023, 2024), and in the case of SPT-CLJ0014-3022 (that is, A2744), we know it is a multiple-merger system. Notwithstanding issues of substructure masking (discussed in Appendix B), it is not surprising to find multiple injection scales. P. L. Gómez et al. (2012) find a bimodal galaxy distribution in SPT-CLJ2248-4431 (AS1063) and infer that it is in a merging state, while the X-ray

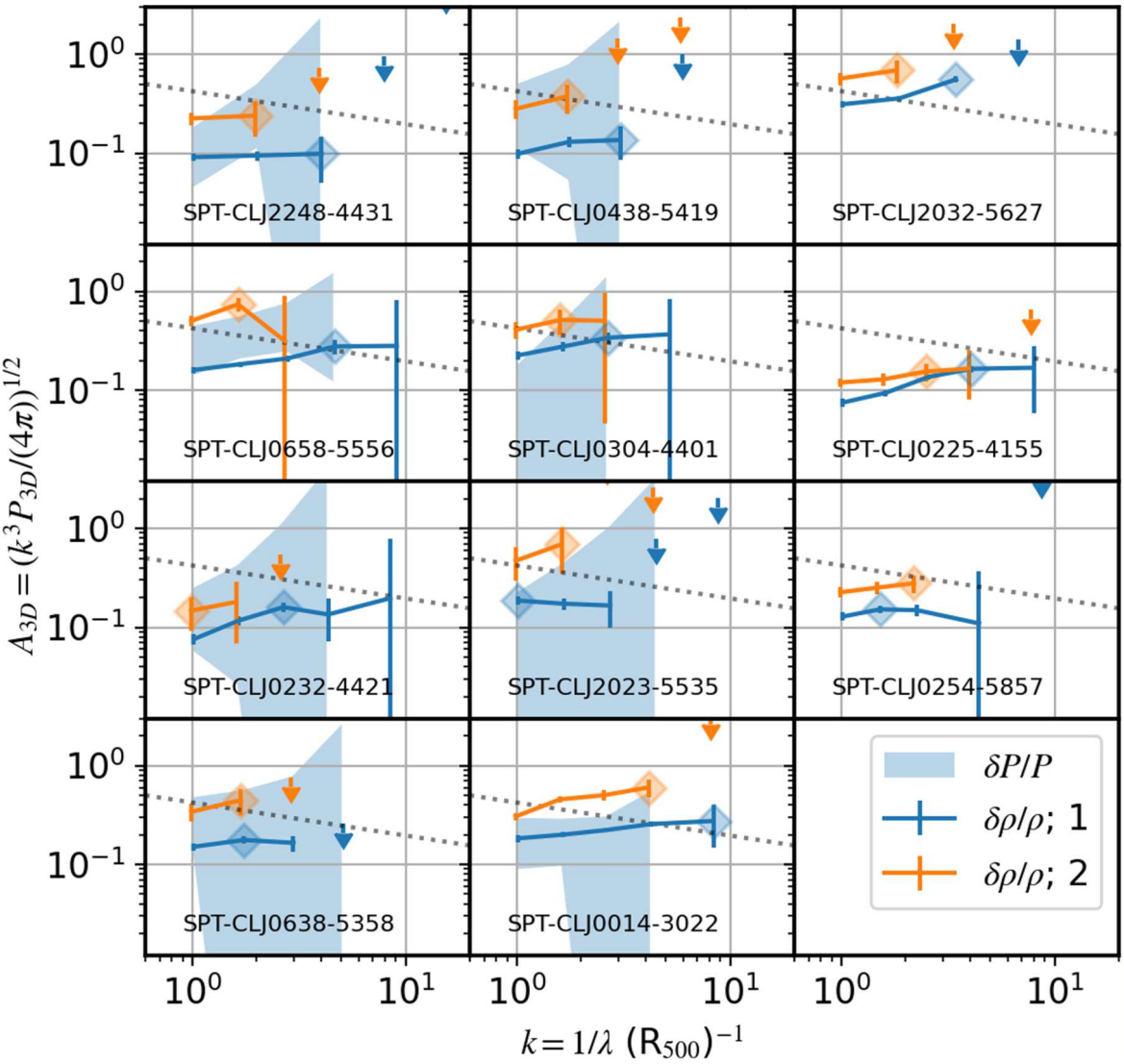

Figure 11. Amplitude spectra of density fluctuations (lines; blue corresponds to Ring 1 and orange to Ring 2) and pressure fluctuations in Ring 1 (shaded region, if significant) for clusters with $\xi > 9$ for at least one node of A_ρ in Ring 1. Diamonds indicate which node is taken as the peak (of nodes with $\xi > 2$). Arrows indicate a 3σ upper limit.

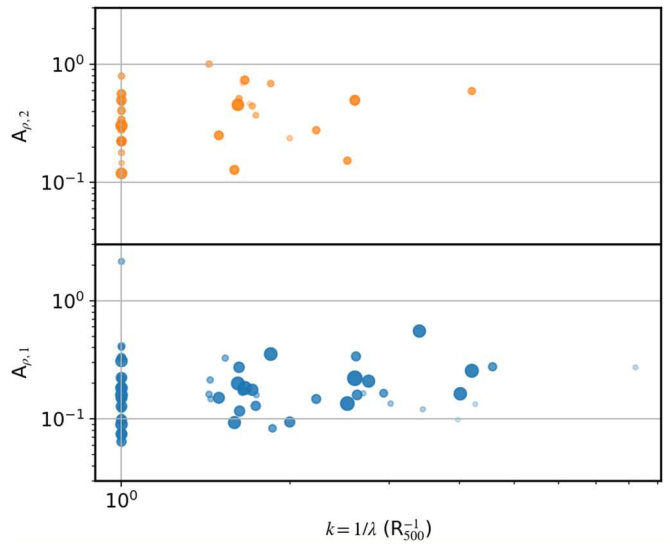

Figure 12. Nodes of amplitude spectra of density fluctuations where A_ρ has significance $\xi > 2$ in the respective Ring. The size and transparency are scaled by the significance such that larger and more opaque points have greater statistical significance.

distribution does not reveal such bimodality. J. A. Shitanishi et al. (2018) classify SPT-CLJ2248-4431 as a non-cool-core cluster and there is no substantial substructure in the X-ray images, including work by V. Olivares et al. (2023), who found no evidence of X-ray cavities in Chandra images of SPT-CLJ2248-4431.

We present all nodes of the amplitude spectra of density fluctuations, A_ρ, with significance $\xi > 2$ in Figure 12. We see a clear trend of fewer points at higher k (smaller scales), given the increased difficulty of placing constraints at these values (see Section 4.3). Even so, we see in Ring 1 (bottom panel of Figure 12) that there appears to be an upward trend in the amplitude spectra. This reflects the notion that the injection scales within Ring 1 are generally smaller than R_{500}. However, an average injection scale in either Ring is fairly unconstrained as we do not see a clear peak/turnover in the amplitude spectra.

Appendix D
Constraints out to R_{500}

We find 15 clusters for which at least one node in the amplitude spectra of density fluctuations within Ring 2 is at least 2σ. The weighted average of the inferred Mach numbers is $\mathcal{M}_{\rho,2} = 0.87$, though the scatter is 0.89, where the distribution is asymmetric. Indeed, many of the systems have inferred gas velocities that are supersonic, which is not expected for turbulent motions alone. If, as before, we exclude those with inferred supersonic gas velocities, we arrive at only four clusters whose weighted average Mach number is $\mathcal{M}_{\rho,2} = 0.59 \pm 18$.

Of the 15 clusters, those that we infer to have supersonic gas velocities are SPT-CLJ0658-5556, SPT-CLJ0638-5358, SPT-CLJ0438-5419, SPT-CLJ0304-4401, SPT-CLJ2023-5535, SPT-CLJ0114-4123, SPT-CLJ0014-3022, SPT-CLJ2341-5119, SPT-CLJ2146-4633, SPT-CLJ2032-5627, and SPT-CLJ0254-5857. Several of these are again known merging clusters where merging structure exists within Ring 2. As stated in Appendix B, masking substructure need not always reduce the inferred fluctuations because the masking can alter the fitted surface brightness profile.

The distribution of inferred $\mathcal{M}_{\rho,2}$ appears bimodal, as did the distribution of $\mathcal{M}_{\rho,1}$. This bimodality may have the same causation as in Ring 1, i.e., seeing turbulence versus substructure, where the latter is due to merging activity and likely corresponds to nonturbulent motions (e.g., shocks). However, we are unable to confidently assert the cause of the apparent bimodality in $\mathcal{M}_{\rho,2}$ due to the fainter X-ray signal in Ring 2. For various significance cuts, we have either three or four clusters with subsonic velocities, where the weighted means of $\mathcal{M}_{3D}$ are between 0.6 and 0.7, which is in agreement with expectations derived in Section 4. That said, better constraints over more clusters are clearly necessary to robustly distinguish between turbulent and nonturbulent motions out to R_{500}.

ORCID iDs

Charles E. Romero https://orcid.org/0000-0001-5725-0359
Massimo Gaspari https://orcid.org/0000-0003-2754-9258
Gerrit Schellenberger https://orcid.org/0000-0002-4962-0740
Bradford A. Benson https://orcid.org/0000-0002-5108-6823
Lindsey E. Bleem https://orcid.org/0000-0001-7665-5079
Esra Bulbul https://orcid.org/0000-0002-7619-5399
William Forman https://orcid.org/0000-0002-9478-1682
Ralph Kraft https://orcid.org/0000-0002-0765-0511
Paul Nulsen https://orcid.org/0000-0003-0297-4493
Christian L. Reichardt https://orcid.org/0000-0003-2226-9169
Arnab Sarkar https://orcid.org/0000-0002-5222-1337
Taweewat Somboonpanyakul https://orcid.org/0000-0003-3521-3631
Yuanyuan Su https://orcid.org/0000-0002-3886-1258

References

Angelinelli, M., Vazza, F., Giocoli, C., et al. 2020, MNRAS, 495, 864
Arévalo, P., Churazov, E., Zhuravleva, I., Hernández-Monteagudo, C., & Revnivtsev, M. 2012, MNRAS, 426, 1793
Astropy Collaboration, Price-Whelan, A. M., Lim, P. L., et al. 2022, ApJ, 935, 167
Astropy Collaboration, Robitaille, T. P., Tollerud, E. J., et al. 2013, A&A, 558, A33
Barret, D., Decourchelle, A., Fabian, A., et al. 2020, AN, 341, 224
Battaglia, N., Bond, J. R., Pfrommer, C., & Sievers, J. L. 2012, ApJ, 758, 74
Beaumont, S., Molin, A., Clerc, N., et al. 2024, A&A, 686, A41
Benson, B. A., Ade, P. A. R., Ahmed, Z., et al. 2014, Proc. SPIE, 9153, 91531P
Bleem, L. E., Crawford, T. M., Ansarinejad, B., et al. 2022, ApJS, 258, 36
Bleem, L. E., Stalder, B., de Haan, T., et al. 2015, ApJS, 216, 27
Bocquet, S., Dietrich, J. P., Schrabback, T., et al. 2019, ApJ, 878, 55
Brunetti, G., & Jones, T. W. 2014, IJMPD, 23, 1430007
Bulbul, E., Chiu, I. N., Mohr, J. J., et al. 2019, ApJ, 871, 50
Churazov, E., Vikhlinin, A., Zhuravleva, I., et al. 2012, MNRAS, 421, 1123
Crawford, T., Bleem, L., Benson, B., et al. 2022, SPT-SZ Compton-y Maps of Abell 2744 and Abell S1063, Argonne National Laboratory, IL
Cruise, M., Guainazzi, M., Aird, J., et al. 2025, NatAs, 9, 36
de Haan, T., Benson, B. A., Bleem, L. E., et al. 2016, ApJ, 832, 95
Duchesne, S. W., Johnston-Hollitt, M., Bartalucci, I., Hodgson, T., & Pratt, G. W. 2021, PASA, 38, e005
Dupourqué, S., Clerc, N., Pointecouteau, E., et al. 2023, A&A, 673, A91
Dupourqué, S., Clerc, N., Pointecouteau, E., et al. 2024, A&A, 687, 58
Eckert, D., Gaspari, M., Vazza, F., et al. 2017, ApJL, 843, L29
Foreman-Mackey, D., Hogg, D. W., Lang, D., & Goodman, J. 2013, PASP, 125, 306
Gaspari, M., Brighenti, F., Temi, P., & Ettori, S. 2014a, ApJL, 783, L10
Gaspari, M., & Churazov, E. 2013, A&A, 559, A78

Gaspari, M., Churazov, E., Nagai, D., Lau, E. T., & Zhuravleva, I. 2014b, A&A, 569, A67
Gaspari, M., Eckert, D., Ettori, S., et al. 2019, ApJ, 884, 169
Gaspari, M., Tombesi, F., & Cappi, M. 2020, NatAs, 4, 10
Gómez, P. L., Valkonen, L. E., Romer, A. K., et al. 2012, AJ, 144, 79
Hartigan, J. A., & Hartigan, P. M. 1985, AnSta, 13, 70
Heinrich, A., Zhuravleva, I., Zhang, C., et al. 2024, MNRAS, 528, 7274
Hofmann, F., Sanders, J. S., Nandra, K., Clerc, N., & Gaspari, M. 2016, A&A, 585, A130
Kass, R. E., & Raftery, A. E. 1995, JASA, 90, 773
Kelly, B. C. 2007, ApJ, 665, 1489
Kempner, J. C., & David, L. P. 2004, MNRAS, 349, 385
Khatri, R., & Gaspari, M. 2016, MNRAS, 463, 655
Komarov, S. V., Churazov, E. M., Kunz, M. W., & Schekochihin, A. A. 2016, MNRAS, 460, 467
Kraft, R., Markevitch, M., Kilbourne, C., et al. 2022, arXiv: 2211.09827
Kravtsov, A. V., & Borgani, S. 2012, ARA&A, 50, 353
Lau, E. T., Gaspari, M., Nagai, D., & Coppi, P. 2017, ApJ, 849, 54
Lovisari, L., Ettori, S., Rasia, E., et al. 2024, A&A, 682, A45
Lovisari, L., Forman, W. R., Jones, C., et al. 2017, ApJ, 846, 51
Markevitch, M., Gonzalez, A. H., David, L., et al. 2002, ApJL, 567, L27
McNamara, B. R., & Nulsen, P. E. J. 2012, NJPh, 14, 055023
Meidinger, N., Barbera, M., & Emberger, V. 2012, Proc. SPIE, 10397, 103970V
Nandra, K., Barret, D., Barcons, X., et al. 2013, arXiv: 1306.2307
Nelson, K., Lau, E. T., & Nagai, D. 2014, ApJ, 792, 25
Olivares, V., Su, Y., Forman, W., et al. 2023, ApJ, 954, 56
Pasini, T., De Gasperin, F., Brüggen, M., et al. 2024, A&A, 689, A218
Plagge, T., Benson, B. A., Ade, P. A. R., et al. 2010, ApJ, 716, 1118
Pratt, G. W., Arnaud, M., Biviano, A., et al. 2019, SSRv, 215, 25
Raja, R., Rahaman, M., Datta, A., et al. 2021, MNRAS, 500, 2236
Rau, A., Meidinger, N., Nandra, K., et al. 2013, arXiv: 1308.6785
Romero, C. E. 2024, ApJ, 975, 197
Romero, C. E., Gaspari, M., Schellenberger, G., et al. 2023, ApJ, 951, 41
Romero, C. E., Gaspari, M., Schellenberger, G., et al. 2024, ApJ, 970, 73
Schuecker, P., Finoguenov, A., Miniati, F., Böhringer, H., & Briel, U. G. 2004, A&A, 426, 387
Shi, X., Nagai, D., Aung, H., & Wetzel, A. 2020, MNRAS, 495, 784
Shitanishi, J. A., Pierpaoli, E., Sayers, J., et al. 2018, MNRAS, 481, 749
Simionescu, A., ZuHone, J., Zhuravleva, I., et al. 2019, SSRv, 215, 24
Simonte, M., Vazza, F., Brighenti, F., et al. 2022, A&A, 658, A149
Snowden, S. L., Mushotzky, R. F., Kuntz, K. D., & Davis, D. S. 2008, A&A, 478, 615
Sunyaev, R. A., & Zel'dovich, Y. B. 1972, CoASP, 4, 173
The Astropy Collaboration 2018, astropy v3.0.5: A Core Python Package for Astronomy, Zenodo, doi:10.5281/zenodo.1461536
van Weeren, R. J., de Gasperin, F., Akamatsu, H., et al. 2019, SSRv, 215, 16
Voit, G. M., Meece, G., Li, Y., et al. 2017, ApJ, 845, 80
Wittor, D., & Gaspari, M. 2020, MNRAS, 498, 4983
Wittor, D., & Gaspari, M. 2023, MNRAS, 521, L79
XRISM Science Team 2020, arXiv: 2003.04962
Yuan, Z. S., Han, J. L., & Wen, Z. L. 2022, MNRAS, 513, 3013
Zhuravleva, I., Chen, M. C., Churazov, E., et al. 2023, MNRAS, 520, 5157
Zhuravleva, I., Churazov, E., Arévalo, P., et al. 2015, MNRAS, 450, 4184
Zhuravleva, I., Churazov, E. M., Schekochihin, A. A., et al. 2014, ApJL, 788, L13
ZuHone, J. A., Kunz, M. W., Markevitch, M., Stone, J. M., & Biffi, V. 2015, ApJ, 798, 90